Architecture-Driven Digital Image Correlation Technique (ADDICT) for the measurement of sub-cellular kinematic fields in speckle-free cellular materials

Ali Rouwane, Robin Bouclier, Jean-Charles Passieux, Jean-Noël Périé

Architecture-Driven Digital Image Correlation Technique (ADDICT) for the measurement of sub-cellular kinematic fields in speckle-free cellular materials

Ali Rouwane[a,b,*], Robin Bouclier[a,b], Jean-Charles Passieux[a], Jean-Noël Périé[a]

[a]*Institut Clément Ader (ICA), Université de Toulouse, INSA-ISAE-Mines Albi-UPS-CNRS, Toulouse, France*

[b]*Institut de Mathématiques de Toulouse (IMT), Université de Toulouse, UPS-UT1-UT2-INSA-CNRS, Toulouse, France*

Abstract

Measuring displacement and strain fields at low observable scales of complex microstructures still remains a challenge in experimental mechanics often because of the combination of low definition images with poor texture at this scale. This is the case for cellular materials, for which complex local phenomena can occur. The aim of this paper is to design and validate numerically and experimentally a Digital Image Correlation (DIC) technique for the measurement of local displacement fields of samples with complex cellular geometries (*i.e* samples presenting multiple random holes). It consists of a DIC method assisted with a physically sound weak regularization using an elastic B-spline image-based model. This technique introduces a separation of scales above which DIC is dominant and below which it is assisted with image-based modeling. Several *in-silico* experimentations are performed in order to finely analyze the influence of the introduced regularization lengths for different input mechanical behaviors (elastic, elasto-plastic and geometrically non-linear) and in comparison with true error quantification. We show that the method can estimate complex local displacement and strain fields with speckle-free low definition images, even in non-linear regimes such as local buckling or plasticity. Finally, an experimental validation is proposed in 2D-DIC to allow for the comparison of the proposed method on low resolution speckle-free images with a classic DIC on speckled high resolution images.

Keywords: Elastic Image registration, Finite element DIC, Free-form deformation models,

*Corresponding author

Email addresses: ali.rouwane@univ-tlse3.fr (Ali Rouwane), robin.bouclier@math.univ-toulouse.fr (Robin Bouclier), passieux@insa-toulouse.fr (Jean-Charles Passieux), jean-noel.perie@iut-tlse3.fr (Jean-Noël Périé)

Image-based models, B-splines, Isogeometric analysis

1. Introduction

The development of volume imaging opens up attractive horizons in the field of the mechanical characterization of materials, and in particular of architectured materials [1]. X-ray tomography, in particular, currently makes it possible to reveal the internal architecture of certain materials at a micrometric scale [2], or even information on the microstructure of metallic materials [3, 4]. The reconstructed volumetric images are therefore commonly used to build so-called Digital Image-Based (DIB) models [5, 6, 7, 8, 9]. Furthermore, by using *in situ* testing machines [10], it is possible to assess the effects of loading on internal deformation at various scales [11] or damage [2]. In this context, digital volume correlation (DVC) is now commonly used to obtain a 3D displacement field from a sequence of absorption contrast tomographic images [12]. It is then tempting to take advantage of such measurements to validate the DIB models, or even to identify the parameters of the model used to describe the behaviour of the constituent material(s). However, such comparisons are usually conducted at low spatial resolution and in the case of an elastic behaviour [13]. One of the challenges in the field of experimental mechanics is indeed to perform such DVC measurements at the micro architecture scale [14, 15]. The reason for this is related to the origin of the texture that can be used for image correlation. The typical materials of interest in this study are single-phase materials with complex micro-scale architecture, such as cellular materials. This may include metallic/polymeric foams, biological tissues (trabecular bones), cell woods, or additive manufacturing materials such as lattice structures, to name a few. As an example, an image of a Rohacell-51 polymetacrylimid closed cell foam microstructure obtained using X-ray micro-tomography is given in Fig. 1.

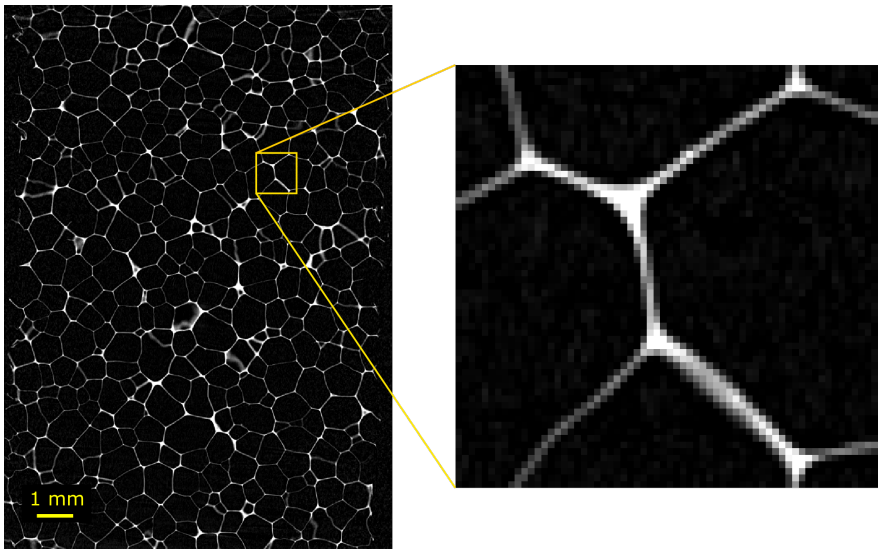

Figure 1: Image of a Rohacell-51 polymetacrylimid closed cell foam microstructure obtained using X-ray micro-tomography. The voxel size is equal to $6\mu m$ and the cell-struts are defined by only 2 to 3 pixels along the thickness direction.

In 2D analysis (DIC or Stereo-DIC), this is possible by artificially adding a high frequency speckle pattern to the observed surface. Numerous techniques exist that allow textures to be deposited over a wide range of scales. However, in volume analysis (DVC), depending on the imaging modality, the variations in grey-levels that generate a DIC suitable texture are associated with the micro architecture and/or the heterogeneity of the constituents. For instance in Fig. 1, the acquisition parameters and the size of the sample were such that the resolution of 6 microns per voxel allows for only 3 voxels on average in the strut thickness. We can see that the struts are not textured at all. Anyway, with such a resolution, one would not even be able to see a sub-cellular speckle, even if it existed. With such microstructures, we are confronted with a paradox: the scale of the constituents is merged with that of the texture, whereas the texture should be defined at a lower scale. This problem has led DVC users to consider elements (global DVC) or subsets (local DVC) of very large size compared to the micro-architecture [12, 16, 17, 18, 19, 20, 15]. The strain fields obtained with such choices are therefore associated with a meso (or macro) scale which is homogenized with respect to the material architecture scale. The lack of texture at a smaller scale precludes

the consideration of smaller elements or subsets, and therefore to access to more resolved measurements. Of course, there have been attempts to deposit texture in volume, especially in manufactured materials using Barium Sulfate [21] or copper particles [22] as contrast agent for instance. But, apart from the fact that it is not easy to guarantee a homogeneous and isotropic texture and that it cannot be generalised to all materials (especially biological ones), this invasive technique may have effects on the behaviour of the material we want to characterize.

This technical barrier which prevents performing strain measurement under the cellular scale represents today's most challenging issue in DVC. For the first time, we propose a method that breaks this barrier and reduces the resolution despite the absence of texture. In order to be able to quantitatively compare the proposed approach (on low resolution images without texture) with a classical method (on high resolution images with painted speckle pattern), we focus in this article on 2D applications. Generalization to 3D, with expected difficulties both in terms of implementation and numerical complexity, will be addressed at a later stage.

The method relies on immersed B-spline image-based mechanical modeling for the automatic and accurate description of the local kinematic of the imaged sample without using the classical meshing procedures [23]. Then we make use of a tuned equilibrium gap method for the weak regularization of the DIC problem [24, 25]. The 2D numerical and experimental tests are performed on a sample that mimics a slice of a cellular foam as the one of Fig. 1. The novelty of our contribution is a measurement method at the scale of the architecture (using the highest possible spatial measurement resolution) and basing it only on the texture of the sample. As it is based on the use of a regularization model representative of the micro architecture of the material, we called our method Architecture-Driven Digital Image Correlation Technique (ADDICT).

As the mechanical response of cellular patterns can be complex and local, the validation of the DIC method must be performed using general mechanical displacement fields that include transformations that are not only reduced to translations and rotations. For this reason, the

suggested DIC validation method consists in generating synthetic images of cellular materials from finite element (FE) simulations and comparing the measured displacement fields to the FE reference displacement field. Although it is possible to consider non-linear regularization models [26], the model used here for weak regularization is elastic. The efficiency of the method to estimate local strain fields of samples undergoing possibly non-linear mechanical behaviours is analyzed considering 3 regimes (elasticity, elasto-plasticity and geometric non-linearity) for the generation of the synthetic images. The Tikhonov-like terms used for the regularization of the DIC problem introduces two parameters that are trade-offs between data fidelity and regularity. A detailed investigation of this trade-off is performed based on a L-curve study [27]. Additionally, the influence of the regularization parameters on the true measurement error is performed. Finally, an experimental validation is performed by comparing the results of proposed method on low resolution speckle-free images with those of a classic DIC on speckled high resolution images.

The present paper is organized as follows: after this introduction, section 2 reviews the foundations of our approach by recalling the DIC problem and its weak regularization. Afterwards, we present the automatic image-based model that allows to obtain the geometric and mechanical descriptions of the cell-struts. Section 3 concerns numerical results that are based on DIC virtual tests using an artificial two-dimensional cellular material. In this section, we firstly compare visually the results of our approach with those of the classical subset method and secondly investigate the influence of the regularization parameters on the measured solution for the three different deformation regimes listed previously. Then, in section 4, the proposed DIC measurement method is assessed through a real tensile test. Finally section 5 concludes on this work by summarizing our main contributions and motivating future research based on the proposed methodology.

2. ADDICT: assisting DIC with mechanical image-based modeling

The proposed ADDICT draws on research dealing with FE-DIC [28, 29, 30, 31, 32], weak mechanical regularization [24, 16, 33, 34], and immersed image-based modeling [8, 35, 9, 23]. This section introduces the main ingredients of the method and accounts for the

choices performed from the current technologies of the literature. More precisely, we start by outlining the foundations, which are related to an enhanced DIC scheme with weak elastic regularization, and then briefly describe the constructed specimen specific image-based model that is the key component of our methodology.

2.1. Foundations: mechanically regularized global DIC

2.1.1. Global DIC

DIC consists in finding the unknown kinematic transformation that conserves the grey-level values of the images taken at different loading steps of a material sample. Within this work, we recall that we restrict ourselves to 2D-DIC but mention that extension to DVC [12, 17, 18] is straightforward from a methodological point of view. More precisely, given two images showing two configurations of a material sample (here let us denote f the image of the material at rest and g the image after load), DIC undertakes to solve the grey-level conservation equation [36]. Mathematically, it reads: find the 2D displacement field $u(x, y)$ such that:

$$f(x, y) = g\left((x, y) + u(x, y)\right), \quad \forall (x, y) \in \Omega, \tag{1}$$

where $\Omega \subset \mathbb{R}^2$ is the ROI, and x and y define the coordinates of any point in the ROI. In practice, the grey-level conservation assumption cannot be guaranteed exactly due to multiple factors (noise, grey-level quantization, sub-pixel interpolation errors...). Therefore, problem (1) is rather solved in a least-squares sense for which a distance of dissimilarity is minimized:

$$u^* = \underset{u \in V}{\arg\min}\, S(u) = \underset{u \in V}{\arg\min}\, \frac{1}{2} \int_\Omega \Big(f(x, y) - g((x, y) + u(x, y)) \Big)^2 dxdy. \tag{2}$$

In order to do so, images f and g need to be somehow interpolated. In this work, a continuous B-spline representation [37] will be used, as specified in section 2.2. The unknown displacement field is searched for in V which is a space spanned by a set of basis functions:

$$u(x, y) = \mathbf{N}(x, y)\mathbf{u}, \tag{3}$$

where $\mathbf{N}(x, y)$ is the considered shape functions matrix and $\mathbf{u} \in \mathbb{R}^{ndof}$ is the total unknown degrees of freedom (dof) vector. Depending on the choice made for $\mathbf{N}$, the DIC methods are divided into two main families: *subset* methods using mostly low-order piecewise polynomials that are discontinuous across the subsets [38, 39, 40, 41], and global methods mainly based on mechanically sound finite elements [28, 29, 42, 43]. Global DIC is considered in this work since this is the starting point to regularize DIC using a mechanical knowledge of the solution. In this context, the basis functions defining V can be chosen, for example, as the standard nodal Lagrange polynomial functions [29, 44, 32], or more regular spline functions in the spirit of free-form deformation models [45, 46, 47] or isogeometric analysis [30, 31, 48, 23]. In any way, these Galerkin approximations introduce a spatial regularization which is related to the size and polynomial degree of the considered finite elements.

Since problem (2) simply consists in a non-linear least-squares problem, it is solved with a Gauss-Newton type algorithm [49]. Given an initial displacement guess $\mathbf{u}^{(0)}$, the solution $\mathbf{u}^{(k)}$ at iteration k is updated as follows:

$$\mathbf{u}^{(k+1)} = \mathbf{u}^{(k)} + \mathbf{d}^{(k)} \quad \text{with} \quad \mathbf{H}_S(\mathbf{u}^{(k)})\mathbf{d}^{(k)} = -\nabla S(\mathbf{u}^{(k)}), \tag{4}$$

where $\nabla S(\mathbf{u}^{(k)})$ is the gradient of S and $\mathbf{H}_S(\mathbf{u}^{(k)})$ is an approximation using only first-order partial derivatives of the Hessian matrix of S. These operators are constructed from image gradients. In the context of the studied images, we perform as usually in the experimental mechanics community; that is, we actually use a modified Gauss-Newton algorithm which consists in approximating the terms $\nabla g((x, y)+u(x, y))$ in the Hessian matrix and the right-hand side by $\nabla f(x, y)$ [49, 50]. This is usually sufficient to capture mechanical kinematic transformations and has the strong benefit to lead to a constant operator $\mathbf{H}_S$, which can thus be inverted once and for all before running the optimization. Further details regarding the implementation of the method can be found in, *e.g.*, [25, 51, 33].

2.1.2. Weak mechanical regularization

As mentioned above, discretization (3) introduces a spatial regularization that can be characterized as a strong regularization in the sense that it is directly related to the size of

the approximation subspace. Roughly speaking, to be able to solve the inverse problem (2), the subset or finite element size must be chosen so that the amount of grey-level data available in a subset or finite element is richer than the corresponding elementary kinematic basis. In the conventionally used subset-DIC framework, the usual rule in this respect is to set a subset size that contains at least 3 speckle dots [52, 53, 54]. For our images of speckle-free cellular type materials, this would lead to a subset size as depicted in Fig. 2 (see also section 3.4 where further details regarding this image are provided). Obviously, the resulting approximation space appears too coarse in view of estimating the kinematic fields at the sub-cellular scale. A finite element mesh as fine as the one of Fig. 2 would be necessary instead but, in this case, the strong regularization would not be sufficient anymore, thereby leading to a singular matrix $\mathbf{H}_S$ in (4).

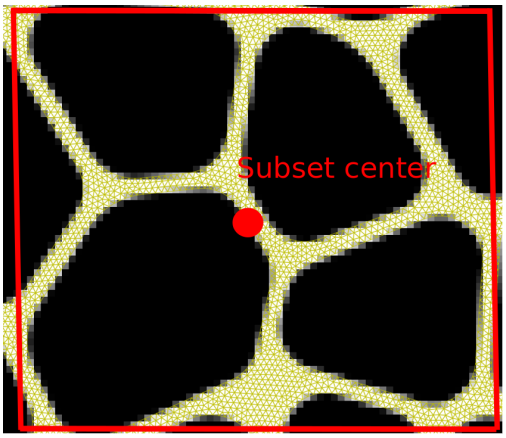

Figure 2: Size of subset (red rectangle) to properly regularize the DIC problem coming from images of speckle-free cellular type materials. The resulting approximation space appears too coarse in view of estimating the kinematic fields at the sub-cellular scale. A finite element mesh as fine as the one depicted in this figure would be necessary instead, thus leading to a severely ill-posed inverse problem.

An alternative approach is to resort to Tikhonov regularization techniques [55]. These are weak regularization schemes that consist in adding to the initial DIC objective function (2) a specific term, based on differential operators, to smooth the solution fields [56, 57, 20, 58]. In particular, it may be proposed within the FE-DIC technology to penalize the L_2-norm of the gradient of each component of the measured field. This technique is often referred

to as the Tikhonov regularization technique in the field [59, 60, 19, 48]. In this work, we will indifferently denote this regularization by the Laplacian-based technique in the sense that it uses the vector Laplacian operator $\mathbf{L}$ [19, 23], see Eq. (5). More interestingly, using finite elements in DIC also offers the opportunity to design mechanically sound Tikhonov-like methods by penalizing the distance between the estimated displacement field and its projection onto the space of expected mechanical solutions [24, 25, 16, 17, 61, 33, 34]). This variant will be classified as the mechanically regularized DIC in this paper. In this work, we use these two regularization schemes together (as in, *e.g.*, [16, 23]): in the part of the ROI where no relevant physical information is available, we perform a Laplacian-based regularization, and in the remaining domain where the discrete mechanical equilibrium can be safely formulated, a mechanically regularized DIC based on an elastic behavior of the specimen is performed.

From a numerical point of view, the Laplacian-based regularization consists in augmenting (2) as follows:

$$\mathbf{u}^* = \underset{\mathbf{u}\in\mathbb{R}^{ndof}}{\arg\min} \Big(S(\mathbf{u}) + \frac{\lambda}{2} ||\mathbf{L}\mathbf{u}||_2^2 \Big), \tag{5}$$

where λ is the weighting parameter. For the mechanically regularized DIC counterpart, equation (2) is rather complemented by the L_2-norm of the internal forces produced by an elastic model (in the spirit of the equilibrium gap method [62]):

$$\mathbf{u}^* = \underset{\mathbf{u}\in\mathbb{R}^{ndof}}{\arg\min} \Big(S(\mathbf{u}) + \frac{\lambda_K}{2} ||\mathbf{D}_K\mathbf{K}(E=1,\nu)\mathbf{u}||_2^2 \Big). \tag{6}$$

The weighting parameter is this time denoted λ_K. $\mathbf{K}$ is the stiffness matrix of an isotropic and homogeneous elastic model defined at the sub-cellular scale of the material. The associated Young's modulus E is fixed to 1 as $\mathbf{K}$ is proportional to E (the influence of E is thus taken into account through λ_K). $\mathbf{D}_K$ is a boolean dof selection operator that selects the dof located in the bulk and on the free edges. Such a dof selection appears necessary because we do not know well the Dirichlet and non-zero Neumann boundary conditions (in practice, we may barely access to a resultant in one direction). Finally, we combine both schemes (5) and (6) to regularize each dof of the unknown measured field, which leads to the following enhanced

DIC problem:

$$\mathbf{u}^* = \underset{\mathbf{u}\in\mathbb{R}^{ndof}}{\arg\min} \Big(S(\mathbf{u}) + \frac{\lambda_K}{2} ||\mathbf{D}_K \mathbf{K}(E=1,\nu)\mathbf{u}||_2^2 + \frac{\lambda_L}{2} ||\mathbf{D}_L \mathbf{L}\mathbf{u}||_2^2 \Big), \tag{7}$$

where operator $\mathbf{D}_L$ selects the Dirichlet and non-zero Neumann edges of the ROI, and λ_L is the weighting parameter for the Laplacian-based part of the regularization.

Remark 1. *Let us note here that the Dirichlet and non-zero Neumann boundary regularization is only used in order to stabilize the measurement at the boundaries. It uses the Laplacian operator so the only physics prescribed on these boundaries is related to a diffusion problem. For more mechanically sound regularizations on theses boundaries, we refer the reader to other boundary stabilization strategies used in the case of the equilibrium gap method [63, 34].*

Finally, it has to be underlined that the (homogeneous and isotropic) elastic behavior at the sub-cellular scale is not prescribed in a strong way in (7). It is only used as a low pass filter to alleviate oscillatory effects [16, 17]. From a global point of view, we exploit the information coming from the movement of cell boundaries (with $S(\mathbf{u})$ in (7)) and weakly prescribe a locally elastic behavior to softly regularize DIC in the textureless microstructure, which makes sense in continuum mechanics, even for measuring inelastic fields as will be demonstrated in sections 3 and 4. In some sense, such a procedure enables to mitigate the tradeoff between the FE interpolation error (sometimes referred to as model error in DIC) and so-called ultimate random error (that is related to the ill-posedness of the inverse problem) [53, 51]. Overall, when using this regularization, three *a priori* input parameters $(\lambda_K, \lambda_L, \nu)$ influence the DIC measurement quality. In theory, a correct estimation of ν must be provided which remains a problem for this class of methods. However it can be updated [25]. The problem thus focus on the fine tuning of (λ_K, λ_L), which will be addressed in section 3.

2.1.3. Functional normalization and physical regularization lengths

As the different optimization residuals are not normalized in (7), typical values of λ_L and λ_K range from 10^1 to 10^9 and their sensitivity to the measured field is not constant across

this interval. Besides, the link between λ_L and λ_K and physical lengths is not obvious. As a remedy, a mechanical interpretation of these regularization schemes has been introduced in [16, 17]. To start with, a normalization of the residual can be considered using a reference shear wave displacement v, here chosen in the form:

$$v_x(x,y) = \cos\left(\frac{2\pi}{T}y\right), \quad v_y(x,y) = 0, \tag{8}$$

where T is the wave-length. The normalization of the functional (7) consists in dividing each optimization term in (7) by its evaluation at the displacement v. Denoting by $\mathbf{v}$ the dof vector associated to the finite element discretization of v, the descent direction using this normalization is therefore given by the following linear system:

$$\begin{aligned}\left(\mathbf{H}_S + \lambda_K \frac{\mathbf{v}^T\mathbf{H}_S\mathbf{v}}{||\mathbf{D}_K\mathbf{K}\mathbf{v}||_2^2}\mathbf{K}^T\mathbf{D}_K\mathbf{K} + \lambda_L \frac{\mathbf{v}^T\mathbf{H}_S\mathbf{v}}{||\mathbf{D}_L\mathbf{L}\mathbf{v}||_2^2}\mathbf{L}^T\mathbf{D}_L\mathbf{L}\right)\mathbf{d}^{(k)} = \\ -\nabla S(\mathbf{u}^{(k)}) - \left(\lambda_K \frac{\mathbf{v}^T\mathbf{H}_S\mathbf{v}}{||\mathbf{D}_K\mathbf{K}\mathbf{v}||_2^2}\mathbf{K}^T\mathbf{D}_K\mathbf{K} + \lambda_L \frac{\mathbf{v}^T\mathbf{H}\mathbf{v}}{||\mathbf{D}_L\mathbf{L}\mathbf{v}||_2^2}\mathbf{L}^T\mathbf{D}_L\mathbf{L}\right)\mathbf{u}^{(k)}.\end{aligned} \tag{9}$$

Let us note at this stage that the left-hand side operator still remains constant and only the right-hand side is updated during the optimization iterations. Using spectral analysis, it can be shown that the linear operators $\mathbf{L}$ and $\mathbf{K}$ used for regularization can be interpreted as low-pass filters (see, again, [16, 17]). More precisely, regularizing using the L_2-norm of the second-order differential operators $\mathbf{L}$ and $\mathbf{K}$ can be seen as a fourth-order low-pass filter acting on the measured displacements on both the bulk and boundary regions. As a result, the regularization weights λ_L and λ_K can be related to cut-off characteristic lengths denoted l_K and l_L which verify:

$$\lambda_K = \left(\frac{l_K}{T}\right)^4, \quad \lambda_L = \left(\frac{l_L}{T}\right)^4. \tag{10}$$

As λ_K and λ_L are dimensionless, the characteristic lengths l_K and l_L have the same unit as the period T of the shear wave which is in pixels. For a proper study and a mechanical interpretation of the implemented methodology, the regularization weights will be tuned in this paper by changing the values of the cut-off wave-lengths l_K and l_L (see section 3 in particular). The value of parameter T has no real influence on the results: it is just requested

to take it large enough so that the wave v can be accurately described by the considered finite element mesh (at least T should be equal to 4 element lengths).

2.2. Specimen specific regularization using an immersed B-spline image-based model

The main feature of our solver (9) is to make use of a stiffness matrix accounting for the cellular architecture to drive DIC within the struts and/or walls of the material. Building such a stiffness matrix requires to investigate the field of image-based modeling which aims at performing mechanical simulation directly on grey-scale data. In this work, we propose to make use of the advanced immersed B-spline image-based model built in [23] which has the interest of being fully automatic, higher accurate and with a proper description of strain fields compared to more standard voxel-based approaches [7, 64], and fairly-priced in the sense that it provides the best possible accuracy (bounded by pixelation errors) while ensuring minimal complexity.

2.2.1. Construction of the automatic and fairly-priced image-based model

We now briefly review the construction of the considered image-based model. Only the fundamentals are given here. For further details, the interested reader is referred to [23] and the works cited hereafter. The model is based on three main ingredients: (i) a level-set characterization of the boundary [9], (ii) a higher-order spline fictitious domain analysis approach, often referred to as the isogeometric Finite Cell Method (FCM) [35] in the field, and (iii) a fine tuning of the related discretization parameters (quadrature rule, element size, polynomial degree) to make it fairly-priced.

More precisely, Fig. 3 summarizes the different steps of the construction of the model.

- First, a level-set characterization of the material's boundary is performed by constructing a binary function that is equal to 1 if the evaluated point is in the region of interest and 0 in void areas (see Fig. 3a). In order to do so, we apply the simple and robust strategy of [9] that consists in building a smooth B-spline representation of the image and obtaining a regular contour of the boundary by taking an iso-value of the

representation.

- In a second step, the region of interest is embedded in a structured smooth and higher-order B-spline grid for the discretization of the measured displacement field (see Fig. 3b). The matrix $\mathbf{N}$ in (3) contains therefore B-spline basis functions whose supports are dissociated from the actual geometry. This is the key point of fictitious domain techniques that allow for great accuracy and flexibility in image-based modeling. Resorting to smooth B-spline functions is also interesting to properly describe derivative fields such as strains.

- In a third step, it is requested to integrate over a restriction of the B-spline grid in order to compute a stiffness matrix related to the physical domain As the level-set characterization is a signed distance, the integration is performed easily by means of a quad-tree decomposition which is widely used in FCM (see, *e.g.*, [65, 8, 35, 9]). Each element of the B-spline grid is divided into four integration elements if it cuts the boundary (see Fig. 3c). The integration elements that do not cut the geometric boundary are integrated with a full Gauss quadrature. This decomposition is repeated until a predefined maximum level is reached. In addition, in order to improve the geometric description, the last cut integration elements are subdivided into integration triangles equipped with an exact quadrature rule (see Fig. 3c again).

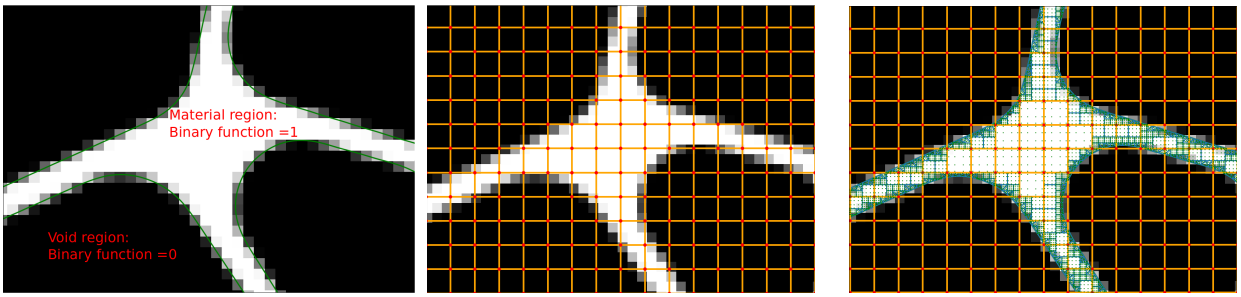

(a) Level-set characterization of the material's boundary.

(b) Embedding of the region of interest in a smooth and higher-order cartesian B-spline grid.

(c) Quad-tree scheme with a closure linear tessellation for defining the domain of integration corresponding to the cell struts (zoomed window *w.r.t.* Figs. 3a and 3b).

Figure 3: Main steps to build the specimen-specific, immersed B-spline image-based model.

The three fictitious domain parameters are adjusted following [23]: the maximum level of quad-tree decomposition is taken so that the minimal size of an integration element is about the same as the pixel size, and smooth cubic B-spline elements of size approximately equal to the cell strut thickness are employed. For illustration purpose, the considered cellular-like specimen is shown in Fig. 4 along with the chosen B-spline mesh that is composed of $n_x = 87$ and $n_y = 64$ elements in the x and y direction, respectively. The corresponding approximate element size is equal to 2.5 pixels.

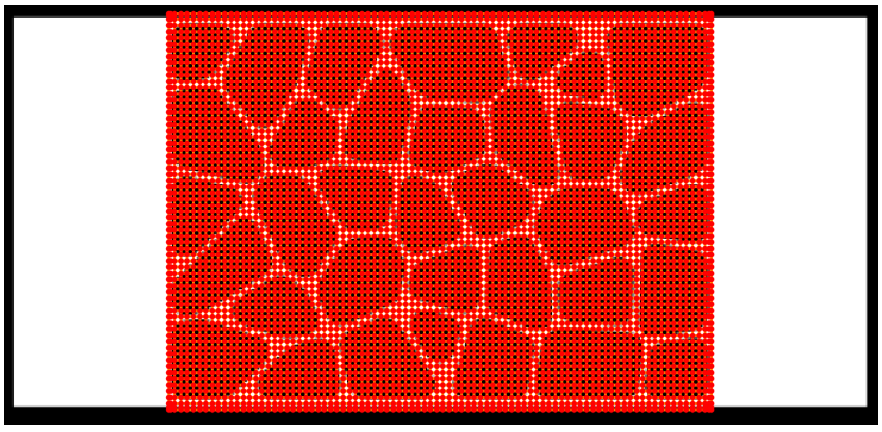

Figure 4: Cubic B-spline grid taken to discretize the measured displacement field for the considered 2D cellular-like specimen.

2.2.2. Conditioning concerns and final fictitious domain DIC approach

In the end, we make use of the B-spline grid and constructed fictitious domain integration rule not only to compute $\mathbf{K}$ but also $\mathbf{H}_S$ and ∇S (and $\mathbf{L}$) in (7). In addition, we interpolate the images by using the smooth B-spline representation constructed at the first step of the image-based model to define the level-set function, which is interesting from a noise and gradient computation point of view [66, 9, 67]. The remaining issue to address is that these operators are in general severely ill-conditioned due to the fact that some basis functions can have their support that do not or slightly intersect the physical domain. As a remedy, we remove the dof corresponding the basis function N_i such that [23]:

$$s(i) = \frac{\displaystyle\int_{Supp(N_i)\cap\Omega} N_i(x,y)dxdy}{\displaystyle\int_{Supp(N_i)} N_i(x,y)dxdy} \leq \varepsilon, \quad (s(i) \in [0,1]), \tag{11}$$

where $Supp(N_i)$ stands for the support of the considered basis function. In this work, we fix $\varepsilon = 10^{-4}$ in order to obtain a good compromise between the conditioning of the left-hand side operator and the accuracy of the solution. In Fig. 5, we show the retained control points after applying (11) with the considered geometry and mesh. Overall, the strategy (7) can be seen as an optimized version, using advanced image-based model techniques, of the mechanically regularized DIC scheme (see, *e.g.*, [24, 16, 17]).

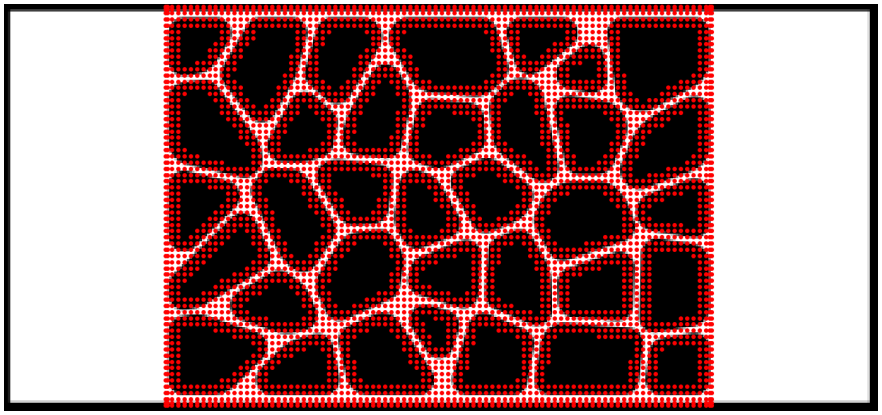

Figure 5: Retained B-spline control points to describe the mechanically regularized DIC solution for the considered 2D cellular-like specimen.

3. Analysis of synthetic images based on virtual tests

In this section, the performance of the proposed speckle-free ADDICT is assessed by analyzing a set of three synthetic test-cases. Namely, given a fine FE mesh fitting the architecture of the cellular material, wisely chosen constitutive properties, and boundary conditions, a displacement field $\mathbf{u}^{\mathbf{fem}}$ is computed from a standard FE analysis, as detailed in section 3.1. Then, synthetic images of the reference and of the deformed configurations are generated, as described in section 3.2. The interest of such virtual tests lies in the fact that the measured fields $\mathbf{u}^{\mathbf{meas}}$ can be compared with the ground truth $\mathbf{u}^{\mathbf{fem}}$ using appropriate measurement errors, see section 3.3. Fig. 6 summarises the process of constructing and analyzing images for our virtual experiment. In addition to performing a virtual elastic test, we will also investigate the ability of our method to estimate local kinematic fields in non-linear regimes (in particular, plasticity and/or geometric non-linearities).

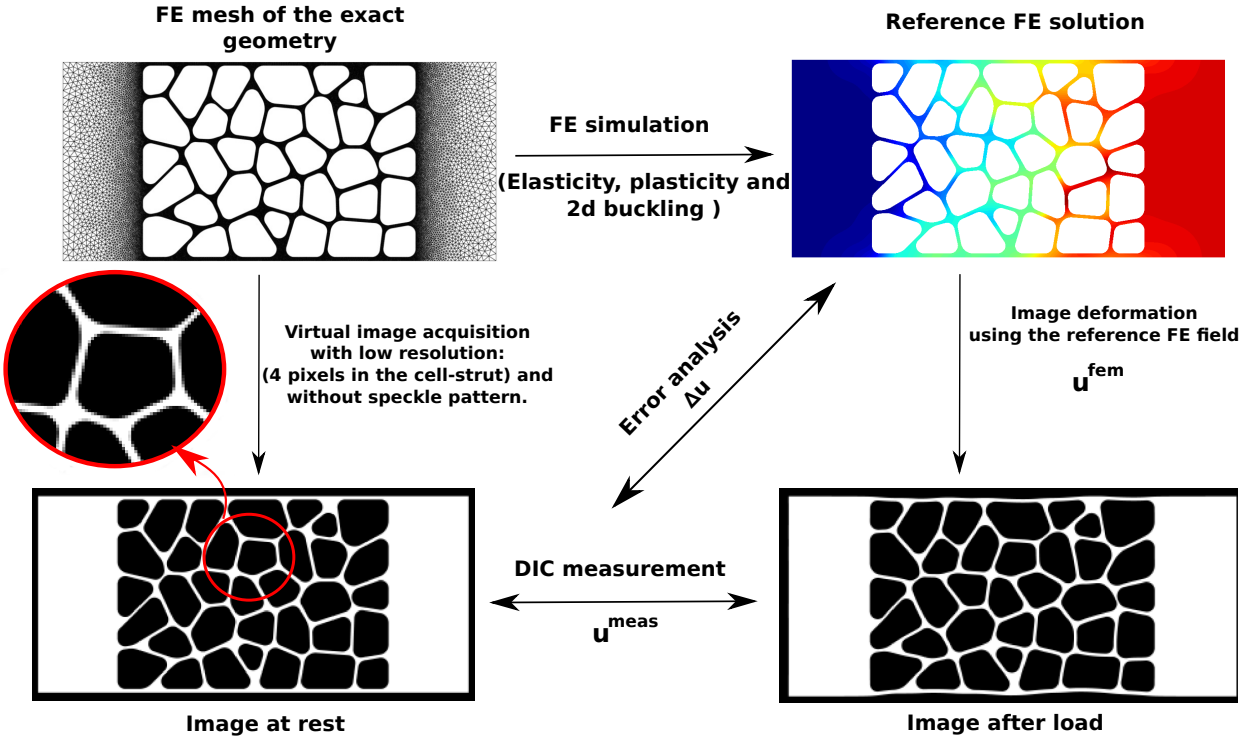

Figure 6: Synthetic image generation and procedure to assess the performance of the DIC measurements.

We proceed as follows for the discussion of the results: in section 3.4, it is shown how challenging it is to estimate sub-cellular kinematic fields with classical subset DIC approaches from such images. The latter are then analyzed with the proposed method. Finally, for each of the three test cases, the influence of the regularization cut-off wave-length is analyzed in section 3.5 based on the so-called L-curves of the optimization problems (5) and (7) and their relation to the true measurement errors.

3.1. Construction of the three virtual tests

For the construction of the reference displacement field $\mathbf{u}^{\mathbf{fem}}$, we considered the mechanical problem depicted in Fig. 7. The left boundary of the sample was fixed ($u_x = u_y = 0$) and an homogeneous displacement was prescribed at the right boundary ($u_y = 0$ and $u_x = u_0$). The top and bottom boundaries were assumed traction-free ($\sigma.n = 0$). The finite element mesh was chosen fine enough to correctly represent the local behavior of the cell struts: approximately six triangular finite elements in a cell strut were considered.

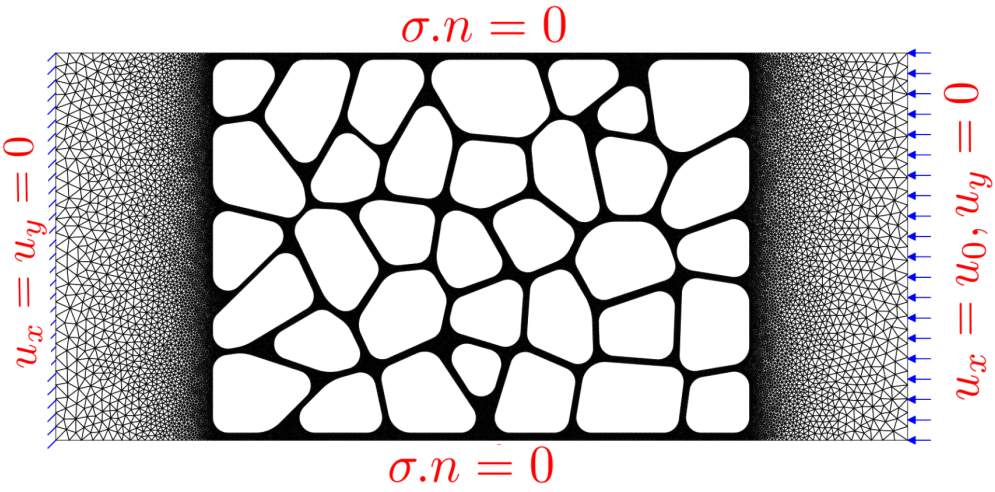

Figure 7: Definition of the virtual experiment: FE mesh of the exact geometric object displayed with the boundary conditions. The sample corners are defined by $x_{min} = 0$ mm, $x_{max} = 110$ mm, $y_{min} = 0$ mm, $y_{max} = 50$ mm.

In this study, three different mechanical regimes were investigated: (i) linear elasticity and (ii) non-linear elasto-plastic constitutive relation under infinitesimal strain theory in

tension ($u_0 > 0$), and (iii) non-linear elasto-plastic constitutive relation under finite strain theory in compression ($u_0 < 0$) including post-buckling. For each regime, a Young's modulus of $E = 187$ GPa and a Poisson coefficient $\nu = 0.3$ were chosen for the sample material. The material's non-linear behavior was based on the piecewise linear hardening law given in Table.1.

Plastic strain	0%	0.2%	1%	10%
Yield stress	230 MPa	295 MPa	340 MPa	425 MPa

Table 1: Elasto-plastic law used for the reference FE simulation.

Figs. 8a-8b-8c show the global force-displacement mechanical response for the three test cases (i), (ii) and (iii), respectively. The red dots correspond to the mechanical states chosen to generate the digital images g in the deformed configuration.

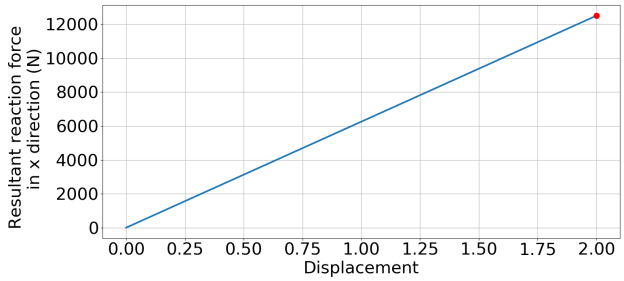

(a) Elastic simulation (tensile test $u_0 > 0$).

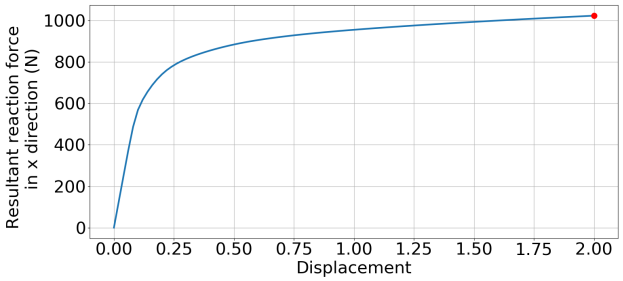

(b) Elasto-plastic simulation (tensile test $u_0 > 0$).

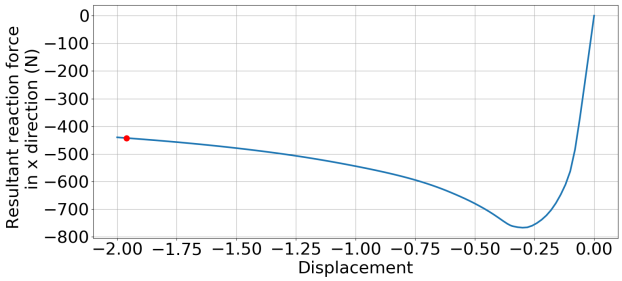

(c) Elasto-plastic simulation with non-linear geometric analysis (compression test $u_0 < 0$).

Figure 8: Evolution of the resultant of reaction forces at the right end of the specimen with respect to the prescribed displacement u_0 in x direction: (a) linear elasticity test (i), (b) elasto-plastic tension test (ii) and (c) geometric non-linear elasto-plastic compression test (iii). The red dots represent the mechanical states used to generate the deformed images.

3.2. Generation of the synthetic images

The virtual DIC testing consists in generating a virtual image of the FE model of Fig. 7 in the load-free configuration f, and another one after loading g from the above computed displacements fields $\mathbf{u}^{\mathbf{fem}}$. In order to mimic the generation of grey-scale images from the geometry of the sample, a first high-resolution binary image is generated using a cartesian grid of pixels over the rectangle with vertices (x_{min}, x_{max}) and (y_{min}, y_{max}). Afterwards, a pixel grey-level value is assigned proportional to its surface fraction to meet the desired low resolution (about 4 pixels in the strut thickness). The same treatment is performed in order to generate the image of the sample in the reference and deformed configurations. This simple rendering method was sufficient in our 2D-DIC analysis whereas other more complex physically sound rendering models could have also been considered, (see, for instance, [68, 51, 69] in the context of Stereo-DIC).

Let us recall that the images are chosen for the loading states corresponding to the red bullets in Fig. 8. For the non-linear regimes (see, in particular, Figs. 8b and 8c), this ensures that the behaviour has clearly entered a non-linear regime. The corresponding images f and g are shown in Fig. 9 for each of the three mechanical problems.

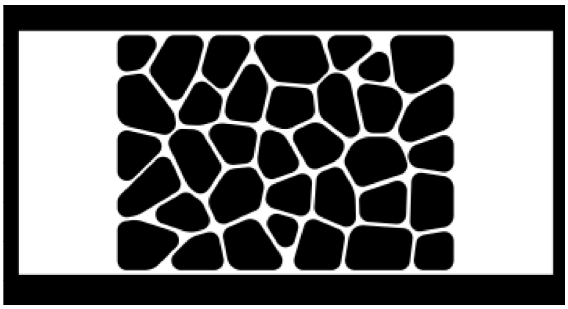

(a) Image of the reference configuration f (load-free).

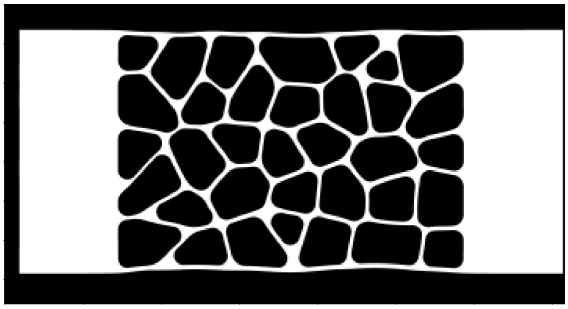

(b) Image of the deformed configuration for the elastic model subjected to tension corresponding to Fig. 8a.

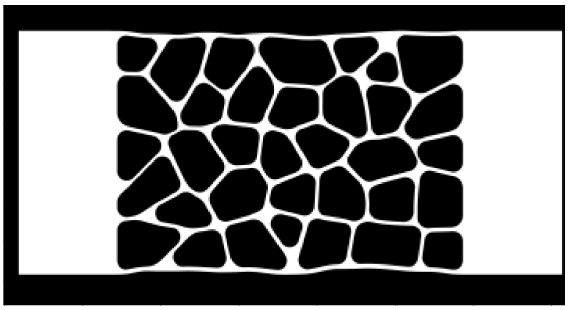

(c) Image of the deformed configuration for the elasto-plastic model subjected to tension corresponding to Fig. 8b.

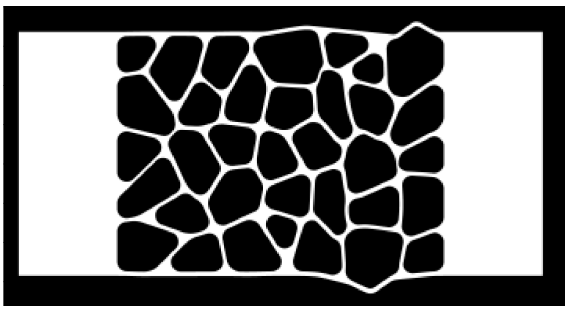

(d) Image of the deformed configuration for the geometrically non-linear elasto-plastic model subjected to compression corresponding to Fig. 8c.

Figure 9: Example of pairs of DIC test images based on the same sample but with different mechanical models. Image dynamic is equal to 255 in the whole image area and equal to 127 in the cell area only.

3.3. Error quantification

As indicated in the overview of the synthetic experimental setup in Fig. 6, the computation of the measurement errors was performed by comparison with the reference FE displacement $\mathbf{u}^{\mathbf{fem}}$ used for generating the synthetic images. Since the reference FE mesh is consistent with the cell geometry, we choose to compute the error between the measured $\mathbf{u}_{\mathbf{x}}^{\mathbf{meas}}, \mathbf{u}_{\mathbf{y}}^{\mathbf{meas}}$ and simulated $\mathbf{u}_{\mathbf{x}}^{\mathbf{fem}}, \mathbf{u}_{\mathbf{y}}^{\mathbf{fem}}$ displacements at the n_p Gauss points defined on all triangular elements of the simulation mesh. In Fig. 10, a zoomed window is provided to see the FE mesh and corresponding integration points located in the image domain. In order to quantify the measurement errors, we consider the measurement uncertainty denoted $\mathcal{U}$. For

instance, for the x-component of the displacement it is defined as follows:

$$\mathcal{U}(u_x) = \sqrt{\frac{1}{n_p - 1} \sum_{i=1}^{n_p} (\mathbf{u_x^{fem}}_i - \mathbf{u_x^{meas}}_i)^2}, \tag{12}$$

where $\mathbf{u}_{xi}$ stands for the evaluation at the i^{th} Gauss point. The uncertainty $\mathcal{U}$ will be used for characterizing the measurement error for u_x and u_y with respect to ground truth.

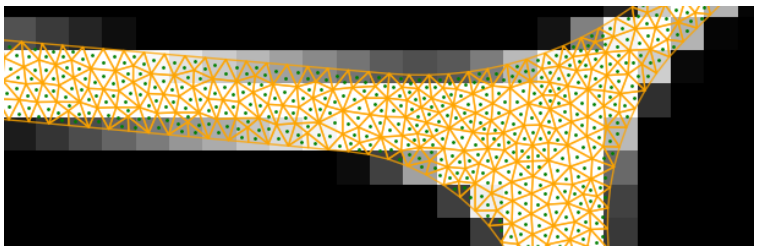

Figure 10: Zoom on an image area. The finite element mesh is superimposed on the image. Green points are the Gauss integration points of the reference triangular FE mesh used for the computation of the error.

3.4. A first analysis vs Subset based DIC

As mentioned in section 2 and illustrated in Fig. 2, the usual practice in subset based DIC/DVC is to set a subset size according to the characteristic length of the image pattern. Based on the auto-correlation function of the image, we can first estimate the microstructure's characteristic length.

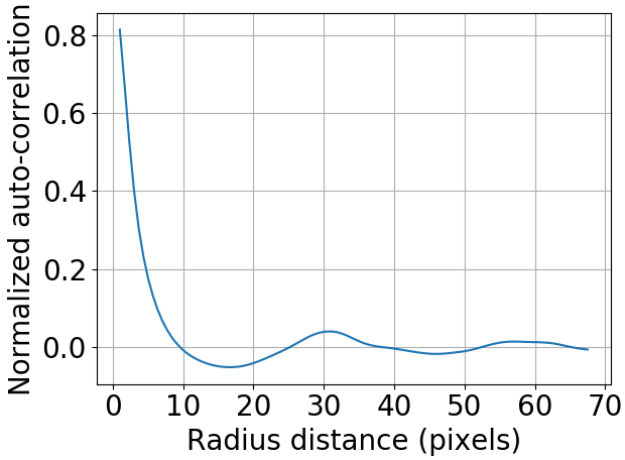

Figure 11: Radially averaged normalized auto-correlation function.

More precisely, by performing the analysis of the evolution of the radially averaged normalized auto-correlation, we can estimate an averaged speckle size in the image and the periods existing thanks to the auto-correlation peaks. The $1/2$ or $1/e$ pre-image of the auto-correlation can characterize the thickness of a cell strut (here around 4 pixels) [53]. The secondary peak at around 30 pixels characterizes the mean cell size. Based on the usual practice in subset DIC [52, 53, 54], it is stated that the subset should contain a minimum of three DIC pattern features, which leads, in our case, to choose very large subset sizes incapable of reconstructing the local kinematic associated to strut bending (see also discussion related to Fig. 2).

As a concrete example, we consider test case (i) where the underlying model is linear elastic. The subset-method was applied with affine subset shape functions. In the case of using the image of Fig. 9a, the subset DIC tool used herein (VIC-2D) suggests an automatic subset size based on the auto-correlation function. A subset size of 63 pixels is suggested in this case (approximately 3 pores per subset as shown by the orange square in Fig. 12), which is consistent with the usual practice. The step size was set to 1. The measurement points are marked by the red dots in Fig. 12. It should be noted that such a large subset size only allows measurement in an area relatively far from the edges.

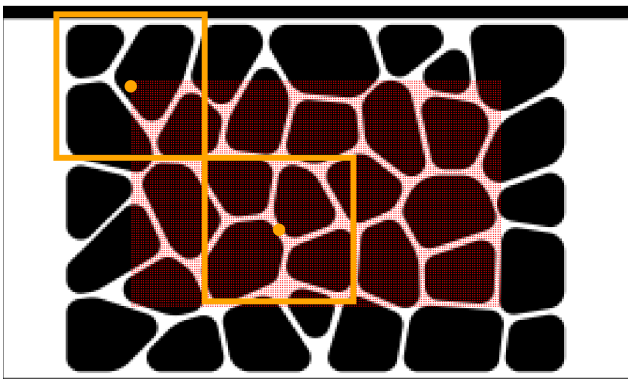

Figure 12: Necessary discretization for the standard subset DIC. The measurement points are marked by the red dots. A large part of the boundary subsets are automatically removed in order to avoid high uncertainty measurements in theses zones. The orange square depicts the subset size.

A visual comparison of the reference (left) and measured (center) displacements and

strains is given in Figs. 13 and 14, respectively. As we are interested by the measurement within the cell struts only, we show the post-processed results in the cell regions using a *a posteriori* binary segmentation. In Fig. 13, it can be seen that the displacement field estimated with the subset method is consistent with the reference field, at least at the macroscopic scale. But when analyzing the field measured by the subset approach in more detail, by looking in particular at the strain field in Fig. 14, we notice that the strain provided by the subset method is completely inconsistent and very far from the reference strain field. More precisely, the obtained strain fields are homogeneous at the scale of the cell-struts and the local bending observed in Fig. 14a is not identified. This shows that large subsets only allow to identify macroscopic (or homogenized) displacements and strain fields.

This problem is due to the difficult compromise in choosing the subset size. Indeed, this parameter alone is used to set both the regularization length and the measurement resolution. This motivates the use of a richer kinematic (small resolution) associated to an alternative regularization technique to better capture the sub-cellular displacement field gradients.

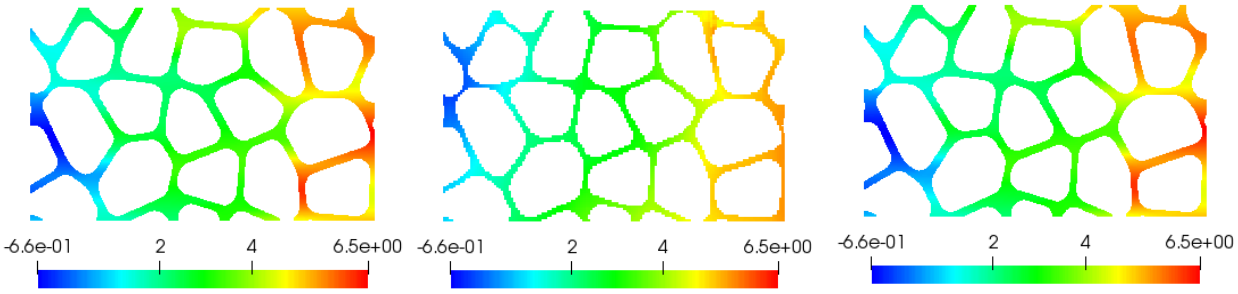

(a) Finite element reference. (b) Subset DIC measurement. (c) Proposed ADDICT measurement.

Figure 13: Horizontal component u_x of the displacement field in the ROI of the subset method (in pixel units).

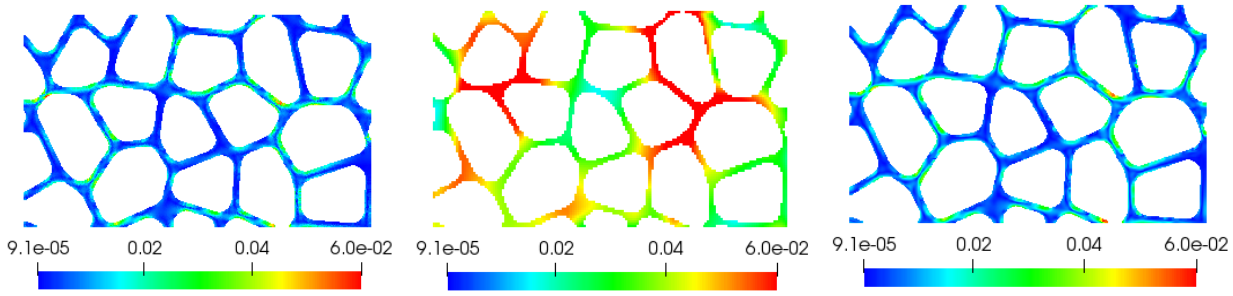

(a) Finite element reference. (b) Subset DIC measurement. (c) Proposed ADDICT measurement.

Figure 14: Plot of the equivalent strain field $\varepsilon_{vm} = \sqrt{\varepsilon_{xx}^2 + \varepsilon_{yy}^2 + 2\varepsilon_{xy}^2}$.

This same set of images is now analyzed with the proposed ADDICT. An image-based model, using a B-spline fictitious domain technology, is constructed from the grey-scale images, as described in section 2.2. This model is used to weakly regularize the FE-DIC problem, as explained in section 2.1 (see, in particular, Eq. (7)). The corresponding measured displacement and strain fields are presented in Figs. 13c and 14c. It can be observed that the displacement field is much better resolved. It shows typical bending gradients which are quite similar to the reference fields. This is a clear illustration of the interest of the FE approach in DIC in its ability to use a mechanical model to improve DIC and to break the aforementioned trade-off.

In the following section we will study the two main parameters of our method: (a) the choice of the regularization lengths l_L and l_K (see Eq. (10)), and (b) the relevance of the model (here linear elastic) used for the regularization operator with respect to the nature of the non-linearity of the measured behaviours.

3.5. Numerical investigation of the influence of the model and parameters used for the regularization

In this section, the influence of the regularization lengths l_L and l_K for different linear and non-linear mechanical regimes is investigated using L-curves. The L-curve study of regularized least-squares problems helps finding the optimal regularization parameter as the one corresponding to the highest curvature point in a log-log plot of the regularization term versus the data fidelity term [27]. For our mechanically regularized scheme (see

Eq. (7)), we thus consider on the horizontal axis the dimensionless data-fidelity term defined by $S(\mathbf{u})/(max(f) - min(f))$, and on the vertical axis the variation of the mechanical equilibrium, *i.e.* such that $||\mathbf{D}_K\mathbf{K}\mathbf{u}^*||_2^2$. In order to investigate the filtering properties of the equilibrium gap based regularization, the plots are performed for different values of the characteristic lengths: l_L and l_K are respectively varied in $[\![0, 40]\!]$ pixels and $[\![0, 200]\!]$ pixels. The L-curve corresponding to the less physically sound Tikhonov variant (5) is also given for comparison purpose regarding the employed regularization model. In a next step, to account for the relevance of the regularization parameters selected with the L-curve approach, a measurement error study (*w.r.t.* ground truth) is carried out. Eventually, several deformed configurations of the material sample are provided with different values of regularization parameters to appreciate visually their influence on the results.

Linear elastic case. First, let us consider the L-curve when regularizing DIC with our approach (7) in case (i), *i.e.* where the synthetic images were generated with a linear elastic model (corresponding to Figs. 8a and 9b). The obtained plot is shown in Fig. 15. The left and right sides of this figure exactly correspond to the same plot, only the colour of the markers changes. On the left, the colour depends on the value of the edge regularization length l_L, and on the right on the bulk elastic regularization length l_K.

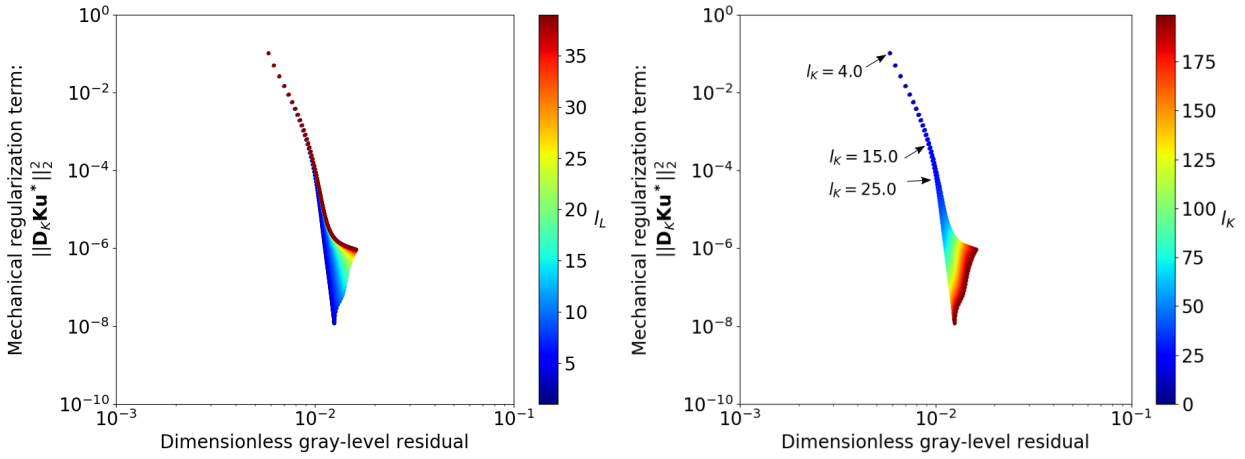

(a) Variation of l_L.

(b) Variation of l_K.

Figure 15: Elastic regularization versus data fidelity for ADDICT on an elastic problem.

The first thing that stands out is that the parameter l_L has very little influence on the L-curve. It only has an effect when the volume elastic regularization parameter l_K is very large (see bottom zone in the figure), which corresponds to very strong regularization. In such a situation, it can be seen as an integrated type DIC method [70] which gives good results provided that (a) the imposed mechanical behaviour in the bulk is the right one (which is the case on this test) and (b) the edge displacements are relevant. This is the reason why edge regularization has an effect in this zone. Fig. 15a shows that l_L should be considered very small (1 to 5 pixels) in order to get an accurate measurement.

Concerning the influence of the bulk regularization given by l_K, while increasing this regularization weight, the equilibrium term keeps decreasing without a significant increase of the grey-level residual (the curve somehow plunges down). This implies that the L-curve does not present a local convexity. The optimal regularization value would be theoretically infinity. This is the typical behaviour of a perfect (here elastic) regularization term. This can be observed since the synthetic example actually exhibits a full linear elastic behavior.

Non-linear cases. The proposed ADDICT with elastic regularization is now applied to the images of test cases (ii) and (iii), *i.e.* with elasto-plastic constitutive relation without and with geometric non-linearities, as shown in Figs. 8b-9c, and 8c-9d, respectively. On Fig. 16a, the corresponding L-curves are presented for the three input models (elastic, elasto-plastic and elasto-plastic with possible geometric non-linearities). Only the influence of l_K is considered, l_L being fixed to its optimal value following previous discussion.

We can now observe three main regions in the L-curve (denoted R1, R2 and R3 in Fig. 16a). On the region R1 (*i.e*, $l_K < 25$), the weight is put more on the grey-level conservation and the standard deviation is higher, the obtained solution is not accurate as will be shown in Fig. 17. Conversely, on the region R3 (*i.e*, $l_K > 30$), the weight is put more on (elastic) regularity. In this case, the grey-level residual increases as the elastic regularity is no longer valid for describing the actual mechanics (here plasticity without or with geometric non-linearities). The choice of l_K must be a compromise between regularity and grey-level conservation. The optimal value for the regularization length is at the point of maximum

curvature [27], i.e. between 25 and 30 pixels, which defined region R2.

Through this study, it can also be emphasized that the L-curve is proving to be an excellent indicator of the relevance of a model in the context of validation [70]. If the L-curve tends to plunges down as the regularization length increases, then the model is probably compatible with the observed mechanical field.

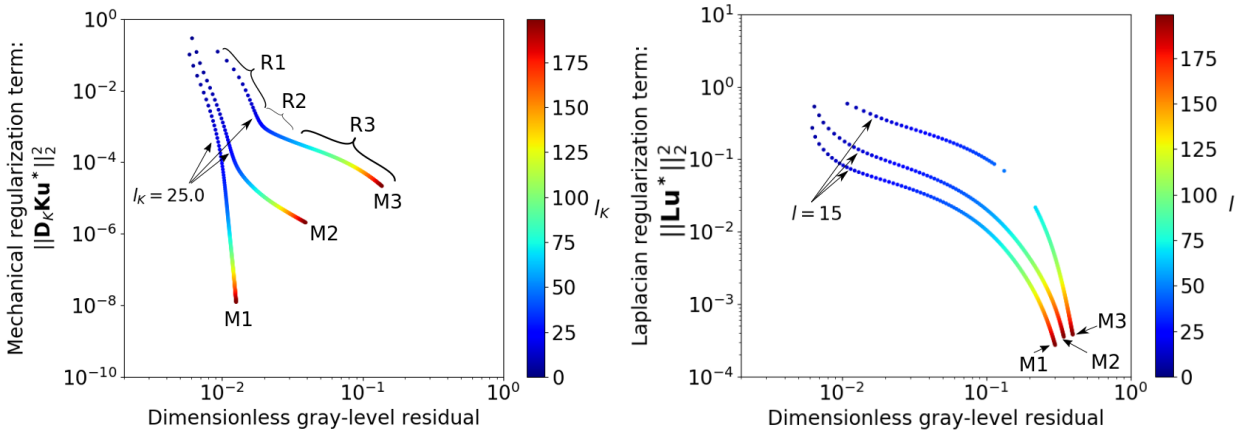

(a) Variation of l_K for the proposed ADDICT. l_L is fixed to its optimal value.

(b) Variation of $\lambda = \left(\frac{l}{T}\right)^4$ (see Eq. (5)) for the Laplacian-based regularization.

Figure 16: Influence of the regularization lengths for the three input models. M1: Elastic model (i), M2: Elasto-plastic model (ii), and M3: Geometrically non-linear elasto-plastic model (iii).

Comparison with a less physically sound regularization kernel. As mentioned above, the choice of the model used for regularization is one of the two important parameters of the approach. Here, the less physically sound Laplacian-based model of Eq. (5) was used to regularize the same set of images. Note that operator $\mathbf{L}$ is built by integrating only on the physical cell struts (*i.e.* avoiding the holes), which differs from the current practice in other fields where such regularization operators are used in both strut and void parts [19, 20]. The corresponding L-curves are given in Fig. 16b. Looking closely at the L-curves of Fig. 16a with the different regularization operators, we can see that the L-curve is clearly more sensitive to the increase of the regularization length when using Laplacian-type regularization as compared to the elastic one.

Link between L-curve and error. In this section, the L-curves are compared to the true errors in order to numerically validate the optimality of the regularization length associated to the maximum curvature. In Fig. 17, the evolution of the measurement error is plotted as a function of the regularization lengths. We recall that, to compute the measurement error defined by (12), the displacement fields are computed on the Gauss-integration points that belong to both the reference finite element geometry and the constructed geometry using the level-set function. First, this figure provides numerical evidence that the optimal value of the regularization calculated from the maximum curvature point also corresponds to the minimum error. Second, this figure also provide numerical evidence that a weak elastic regularization, even when it is not representative of the actual mechanics of the observed specimen, is better than all the other less physical regularization techniques considered in this study, either in a strong way based on polynomials (subset) or in a weak way based on the gradient of the solution (Laplacian).

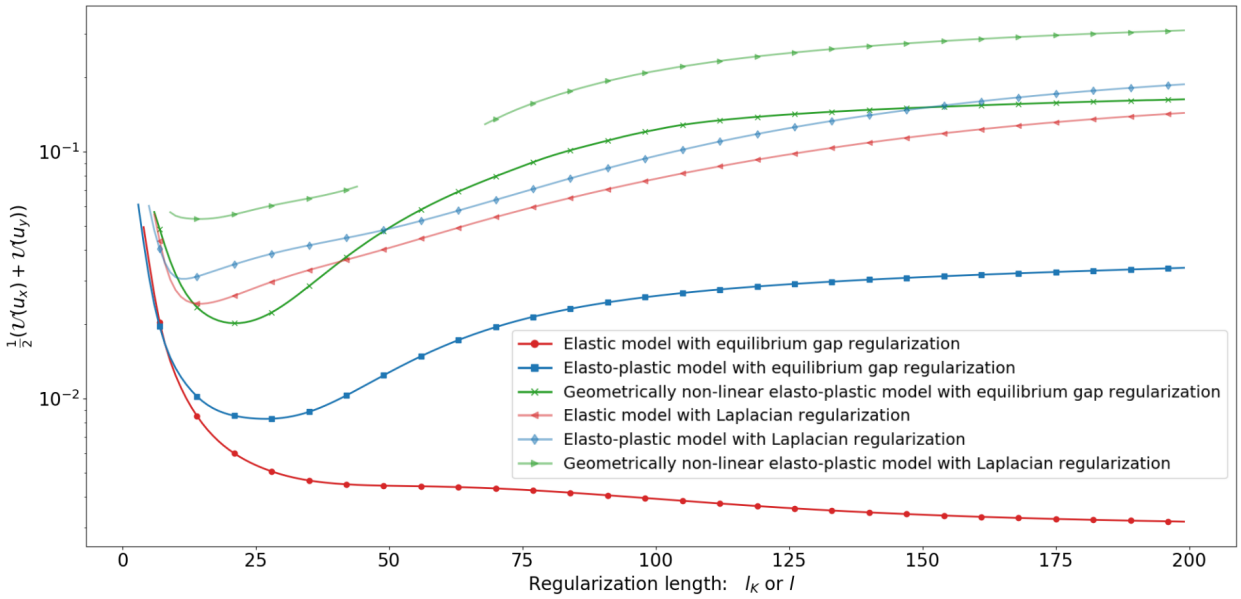

Figure 17: Influence of the regularization parameter on the mean displacement error $(\mathcal{U}(u_x)+\mathcal{U}(u_y))/2$.

Overall, the interpretation that can be made of these results is that the term associated with the grey-level residuals ($S(\mathbf{u})$ in (7)) captures the low frequency part of the solution, here associated with characteristic lengths higher than the cell length ($\approx$ 30 pixels), *i.e.* the

meso scale. In other words, it helps computing the part of the displacement field that aligns the mesh to the edges of the struts. The local part of the displacements, *i.e.* inside the struts or at the micro-scale, which do not modify the grey-level conservation term, are driven by the regularization. It therefore seems consistent that the optimal regularization length is close to the characteristic cell size.

Deformed configurations with different values of regularization parameters. In order to visually appreciate the above interpretation, we eventually show several deformed configurations with different regularization weights. First, considering the elasto-plastic case (ii) (Figs. 8b-9c), we superpose the reference (red) and measured (green) cloud points for a very low regularization (see Fig. 18a) and for an optimal regularization (see Fig. 18b). Following previous discussion, the low regularization allows to satisfy more data fidelity (region R1) and the optimal regularization corresponds to the inflexion point obtained from the results of Fig. 16a (region R2)). When putting more weight on data-fidelity, Fig. 18a shows that non-physical displacements are observed within the cell-struts as the green points move differently than the reference points. Conversely, when considering the optimal regularization weight, the movement inside the cell struts is closer to their reference value, see Fig. 18b where the red and green point clouds are superimposed.

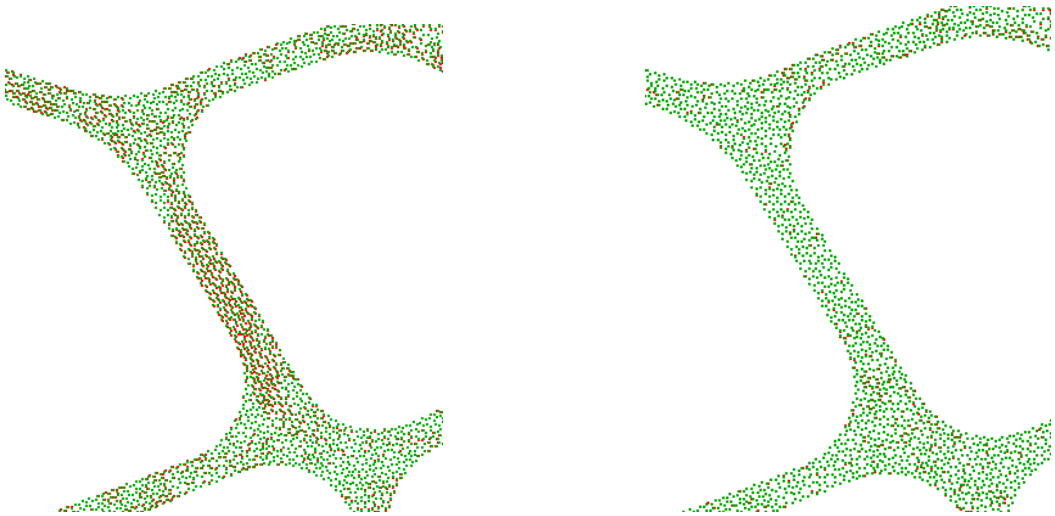

(a) Very low regularization.

(b) Optimal regularization.

Figure 18: Superposition of the deformed point clouds using the reference finite element field (red point cloud) and the measured field using the equilibrium gap method (green point cloud). Figures corresponding to the elasto-plastic problem (ii).

Secondly, in the case of the geometrically non-linear elasto-plastic model (iii) (Figs.8c-9d), when putting a very large weight on the mechanical term (region R3), the correlation fails to correctly represent the geometric non-linearities (see Fig. 19a). In fact, we observe that the regularization model forces the cell struts to bend in an elastic way whereas they should exhibit a post-buckling behavior. When choosing the optimal weight l_K (region R2), the buckling is correctly measured using the same elastic hypothesis for the regularization model, see Fig. 19b. These examples show that even when the observed fields are the response of a more complex behaviour (here geometrically non-linear with elasto-plasticity) than the model used for regularization (here linear elastic), the displacement fields are correctly estimated.

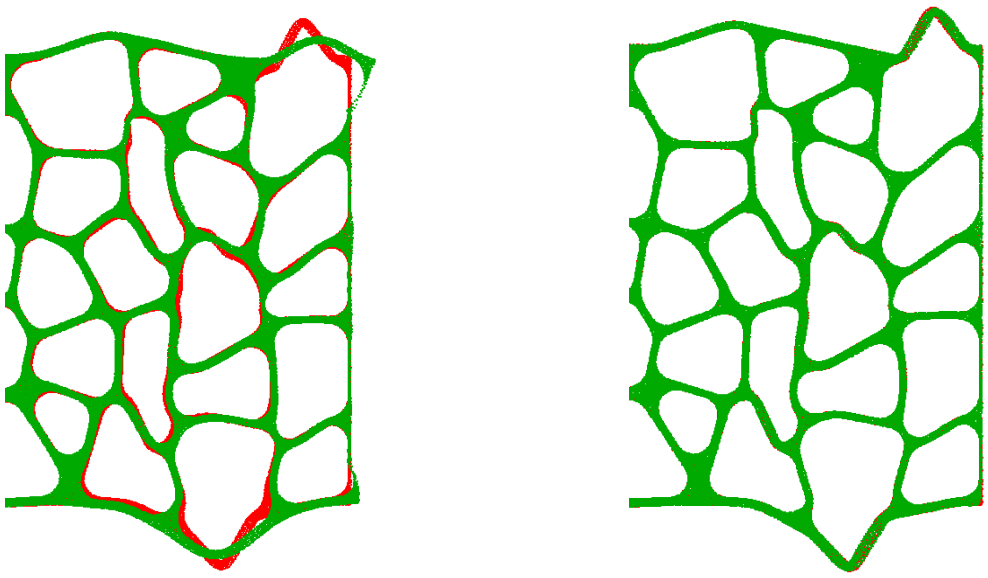

(a) Very high regularization.

(b) Optimal regularization.

Figure 19: Superposition of the deformed point clouds using the reference finite element field (red point cloud) and the measured field using the equilibrium gap method (green point cloud). Figures are corresponding to the geometrically non-linear elasto-plastic problem (iii). (The point clouds are amplified with amplification factor of 2).

Finally, Fig. 20 compares the local distribution of strains in the worst case (geometrically non-linear with elasto-plasticity). Even if the value of the local strain is not totally correct, it is much better than with the other regularization technique considered in this study, and it allows at least the location of high gradient areas.

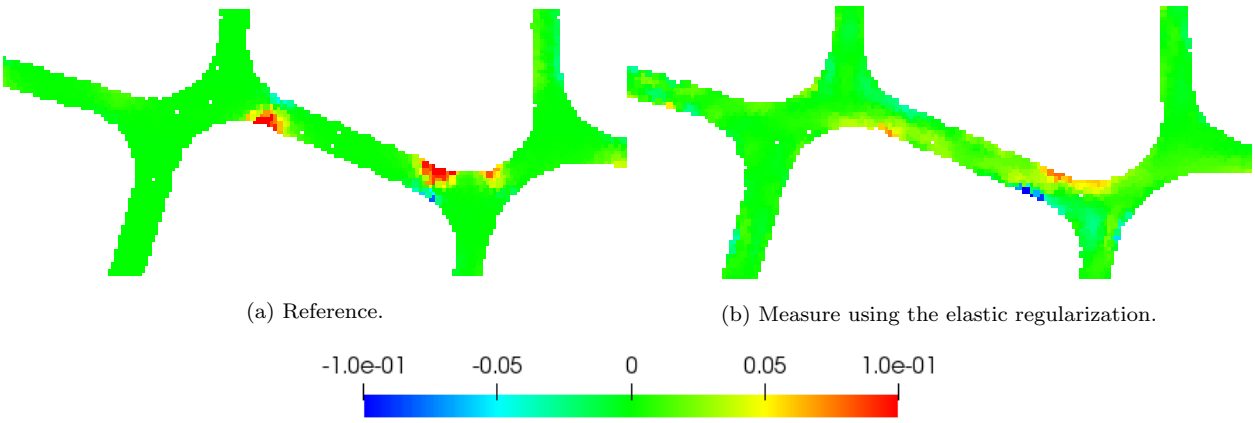

(a) Reference.

(b) Measure using the elastic regularization.

(c) ε_{xx} range values.

Figure 20: ε_{xx} strain.

4. Application to a 2D experiment

We now propose to demonstrate the potential of our ADDICT in an experimental situation where inelastic strains take place. To this end, we have chosen to perform a tensile test on a macroscopic two-dimensional cellular like specimen and to compare the 2D kinematic measurements provided by ADDICT using low-definition speckle-free images of the main side with those obtained by a FE-DIC measurement based on high definition images of the opposite speckled side, considered as the reference (see Fig. 21). A classic FE-DIC approach is here preferred for the reference to obtain a dense continuous displacement everywhere in the struts.

We first chose a suitable geometry, material and production method to build our model material. The geometry adopted is identical to the one used in the previous section (see Fig. 7). The total width of the specimen is 50 mm, and the minimal struts thickness is approximately 0.5 mm. The sample was machined in a 4 mm thick 2024-T3 aluminum sheet from the CAD file using a 5 axis CNC milling machine. This process was preferred to waterjet and laser cutting in order to obtain the desired geometry while minimizing the heat affected zone and avoiding the need to deburr the part. The minimum radii of the fillets were therefore limited in the CAD by the radius of the cutting tool.

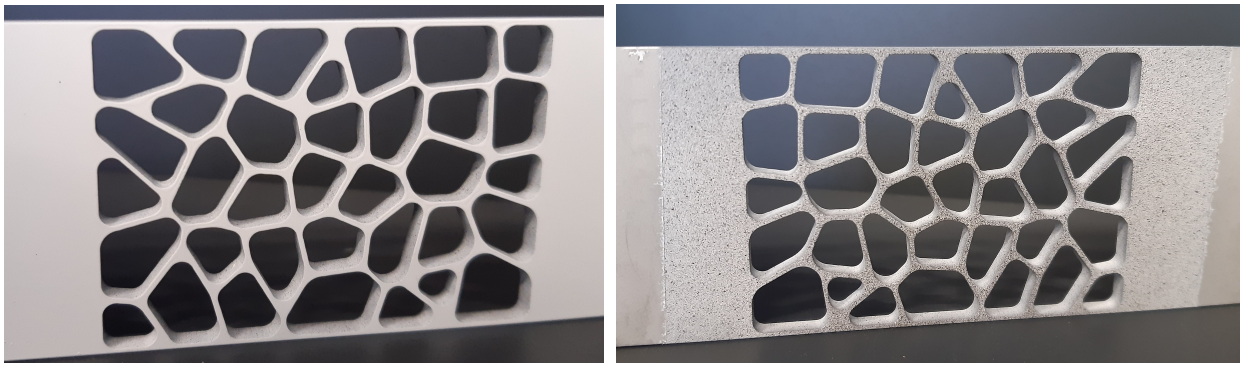

(a) Speckle free side for ADDICT.

(b) Speckled side for reference FE-DIC.

Figure 21: Specimen and preparation for DIC - The 50 mm large sample is milled from a 4 mm 2024-T3 aluminum sheet, then painted white between the regions where it will be fixed in the jaws. One side is simply left as it is, while on the opposite side, a speckle is deposited by means of an airbrush.

Once machined, properly prepared and cleaned, the sample was sprayed with white matt paint in its entire central region, up to the areas that were to be clamped (see Fig. 21a). Then, thin matt black spots were sprayed on the side where FE-DIC measurements were planned (see Fig. 21b). The idea being to capture displacement gradients within the struts thickness, the deposit of this speckle is done here with an airbrush. Fig. 23b shows the distribution of the speckles obtained on the cell sample. The average diameter of the spots is estimated to be around 0.1 mm.

An Instron 8561 100 kN electromechanical tensile machine equipped with a 10 kN cell was used for this test. This machine can be equipped with hydraulic jaws, which avoids accidental twisting of the sample during clamping. Particular care was taken to align the jaws beforehand. The test was carried out under displacement control at a constant displacement rate of 0.12 mm/min.

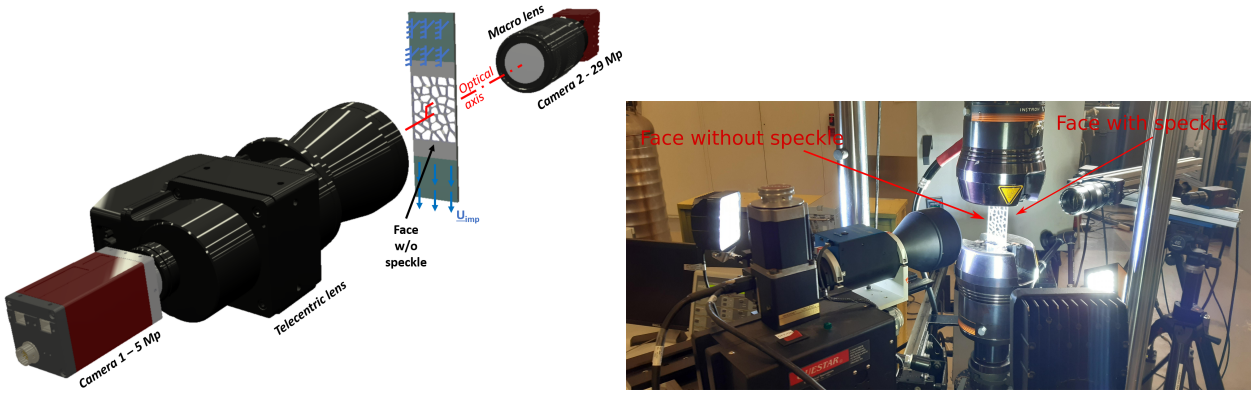

(a) Basic optical setup.

(b) Overview of the experimental setup.

Figure 22: Experimental setup.

The experiment was monitored by multiple cameras triggered using an external TTL square signal. The frame rate was set at 0.2 fps. Fig. 22 shows the basic optical setup chosen for the present analysis. It consists of 2 systems that were very carefully positioned on either side of the sample and oriented (using laser devices) so that the optical axes were perpendicular to the filmed faces. A telecentric lens (Opto Engineering TC ZR 072-C) was used to film the speckle-free side of the sample. This type of lens allow to maintain the magnification independently of the working distance and therefore allow to remove depth effect. It allows here to obtain images of the whole region of interest (field of view: 70.4 mm $\times$52.8 mm). This lens is equipped with a 5Mp CCD camera (Camera 1: Allied Vision Pike). On the opposite side, a 29Mp CCD camera (Camera 2: Allied Vision Prosilica GT6600) equipped with a macro lens (ZEISS PLANAR T 2.0/100 ZF MACRO) were rather selected to retrieve high resolution images of the speckled surface. In this case, the intention was to correctly resolve the small pattern created on the surface. The working distance of the macro lens was set to encompass almost the same region of interest (see Fig. 25). The resulting image has a resolution of about 78 pixels/mm. The zoom presented in Fig. 23b allows to better apprehend the type of texture which are later treated by the FE-DIC. Note that the spots are on average more than 7 pixels, which is a little larger than the value recommended for DIC [54]. The lighting during such an experiment is a problem in itself.

It was indeed tricky to light correctly one side without dazzling the cameras placed on the opposite side. Fig. 22 illustrates how this problem was solved: 2 LED spotlights were used on each side. This same figure reveals an additional stereo DIC bench in the background. The latter allowed us to verify that there was no significant out-of-plane movement during sample clamping or during the test (the maximum out-of-plane displacement measured is at most a few tenths of a millimeter in the gauge region). This feature will consequently no longer be used, or commented on, in what follows.

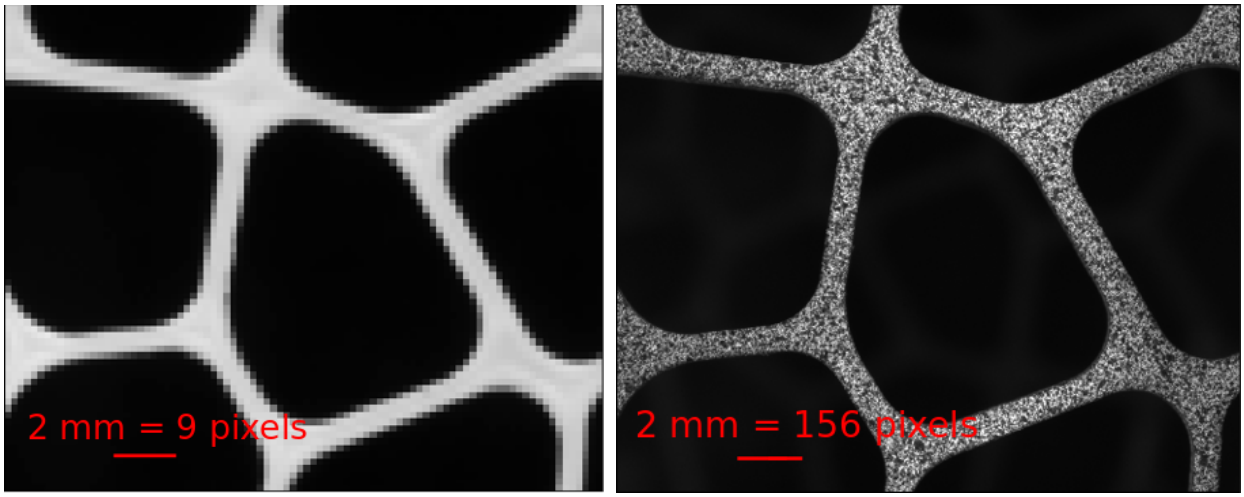

(a) Image of the unspeckled face provided to the ADDICT. Image resolution: 4.5 pixels per mm. Definition of the sub-image presented: 88×73.

(b) Image of the speckled face provided to the FE-DIC. Image resolution: 78 pixels per mm. Definition of the sub-image presented: 1218×1558.

Figure 23: Zoom on a specific region of the sample.

The macroscopic load ($\bar{F}$) - displacement ($\bar{U}$) curve recorded during the experiment is plotted in Fig. 24. The dots indicate when the images were captured. For the DIC analysis which follow, we set the reference image f_i ($i = 1$ unspeckled face, $i = 2$ speckled face) as the first images captured after the mechanical jaws were clamped (point $(\bar{U}, \bar{F}) = (0, 0)$ of the curve in Fig. 24). Up to about 3 kN, the sample exhibit an elastic macroscopic response. Beyond that, the sample undergoes an irreversible strain, highlighted by the discharges. From now on, we will limit ourselves to present the DIC measurements only for a deformed state indicated by the red dot on Fig. 24 (point $(\bar{U}, \bar{F}) = (1.05 \text{ mm}, 4.73kN)$). The total

macroscopic strain is then estimated at 1.5%, while the corresponding residual macroscopic strain is about 0.8%. The corresponding images are then noted g_i.

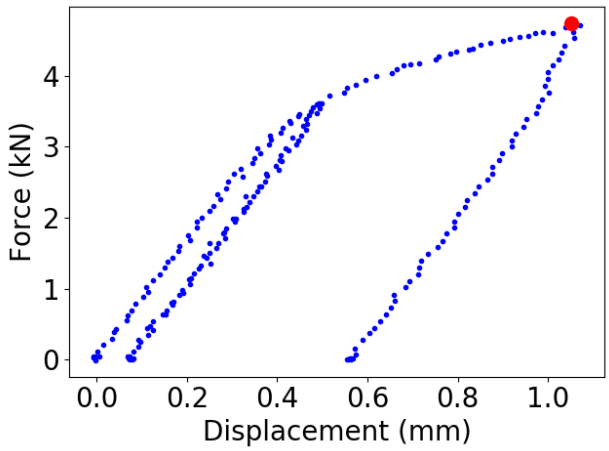

Figure 24: Experimental force ($\bar{F}$)-displacement ($\bar{U}$) curve. Discharges were performed to highlight the non-linear nature of the deformation. Each point corresponds to the acquisition of images. The red one indicates the state that is analyzed in the sequel.

We now propose to measure the displacement fields by image correlation between the reference state (f) and the deformed state (g) images. The recorded images on the speckle-free side (f_1 and g_1) are processed by ADDICT. As we want to test our method in conditions similar to those described above (i.e. with only a few pixels in the strut thickness), the images are downsampled before being processed. Here, we proceed to three successive data binning leading to images of 256 pixel $\times$306 pixels definition (see Fig. 23a). The resolution of the resulting images is then about 4.5 pixels/mm. We then automatically define the implicit geometry of the ROI by building an image-based model as detailed in Section 2.2 (see Fig. 25a). The binary threshold value for the level-set segmentation is here simply set to $(\max(f_1)+\min(f_1))/2$. Since plastic strains are expected, the regularization parameter λ_K is set approximately to the optimal value identified in Fig. 17 of section 3.5. When taking into account the resolution of the experimental images, the corresponding cut-off wave-length is set $l_K = 50$ pixels. This is confirmed by a new study based on the L-curve. Fig. 26 shows that the optimal regularization length lies indeed in the interval $[\![25, 75]\!]$ pixels. For their

part, the high-resolution images (f_2 and g_2) of the speckled side of the specimen are analyzed using the open-source FE-DIC library Pyxel [71]. The unstructured T3 measurement mesh is generated from the very same CAD data used for machining. The average element size is set to 0.2 mm to ensure theoretically that any element encompasses at least one spot. In this 2D configuration, the transformation between the mesh reference frame and the image reference frame (designated projector in this library) is described here with 4 parameters: one rotation around the optical axis, two in plane translations and one scaling. Those parameters are automatically identified by imposing that the projection of nodes on the edges must be aligned with the corresponding edges detected in the images (see Fig. 25b). In practice, we can check that only a few elements do not benefit from grey-scale gradients (see Fig. 29).

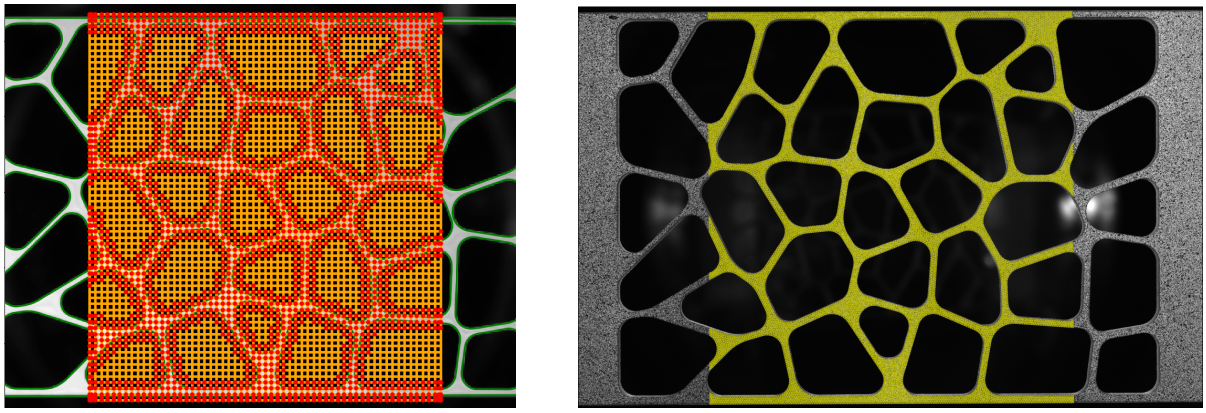

(a) Grid and level-set used to perform ADDICT on the speckle-free face.

(b) FE-DIC mesh used to measure the displacement field on the speckled face.

Figure 25: ADDICT (speckle-free face) and FE-DIC (speckled face) discretizations.

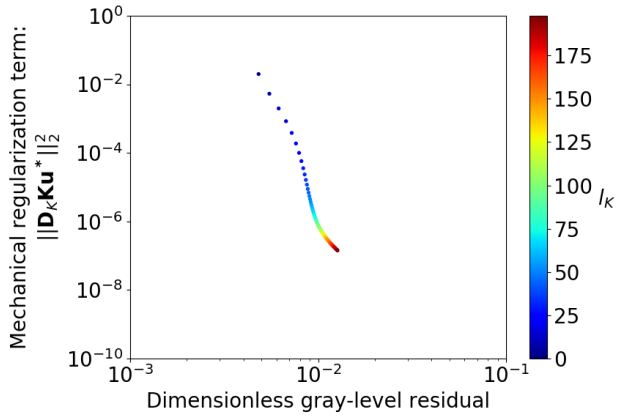

Figure 26: Influence of the regularization lengths for the experimental test-case. Variation of l_K.

The longitudinal displacement u_x and transverse displacement u_y fields measured by ADDICT (exponent 1) and FE-DIC (exponent 2) are respectively compared in Figs. 27 and 28. The maps provided by the two techniques are practically indistinguishable to the naked eye.

A quantitative analysis based on the hypothesis of 2D kinematics is now proposed. In the present situation, as in section 3, we can indeed directly project the displacement fields provided by ADDICT on the integration points of the FE-DIC technique (see Fig. 29). Fig. 30 presents the relative difference between the ADDICT and the FE-DIC measurements $\frac{|u^1 - u^2|}{\bar{U}}$, where $\bar{U}$ stands for the imposed grips displacement. In no case do the observed differences exceed 3% of $\bar{U}$. The local fluctuations for both components are explained by the uncertainty of the FE-DIC measurement. To complete these comparisons, we propose to look at the strains inside the struts (see Fig. 31). Not surprisingly, the regularized measurement leads to less noisy strains and less sharp gradients. Nevertheless, ADDICT allows us to correctly locate the most severely strained regions. In general, we note that the largest deviations are observed on the left and right edges of the ROI. This was expected and is due to the non-physical regularization required on these edges to force ADDICT to converge. The information provided in the immediate vicinity of these regions should therefore be taken with caution.

In addition to the relevance of the results provided, it should be noted that the use of

653 ADDICT does not require any wizardly parameterisation. Indeed, it should be remembered
654 that the behaviour chosen for the regularization is elastic, and no optimization of the gray
655 level threshold to adjust the position of the level-set has been performed (i.e. the description
656 of the geometry has not be optimized - see Fig. 29).

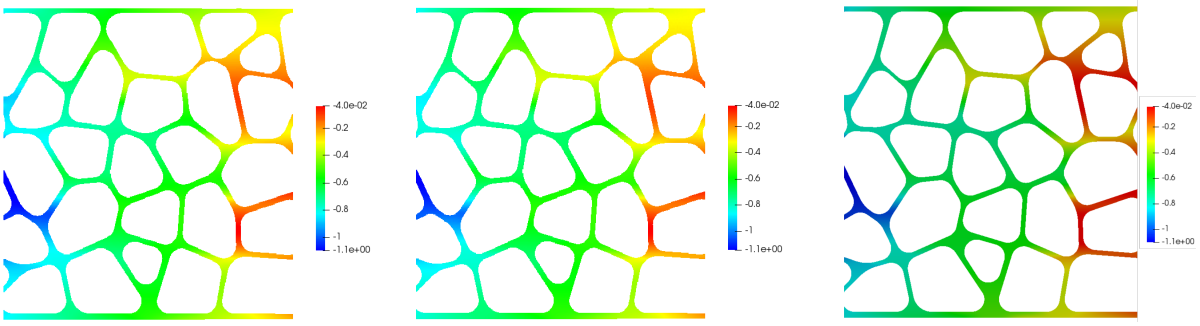

(a) ADDICT measurements with low resolution speckle-free images.

(b) FE-DIC measurement with high resolution speckled images.

(c) FE displacement field computed with Abaqus.

Figure 27: Comparison of the longitudinal displacement fields u_x(mm) measured with ADDICT (u^1), FE-DIC (u^2) and computed with Abaqus (section 3.1) for an imposed displacement $\bar{U} = 1.05$ (Fig. 7).

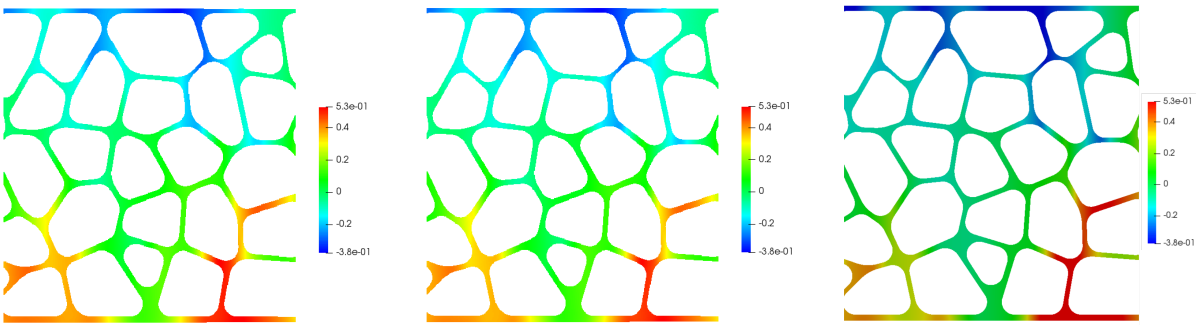

(a) ADDICT measurements with low resolution speckle-free images.

(b) FE-DIC measurement with high resolution speckled images.

(c) FE displacement field computed with Abaqus.

Figure 28: Comparison of the transverse displacement fields u_y(mm) measured by ADDICT (u^1), FE-DIC (u^2) and computed with Abaqus (section 3.1) for an imposed displacement $\bar{U} = 1.05$ (Fig. 7).

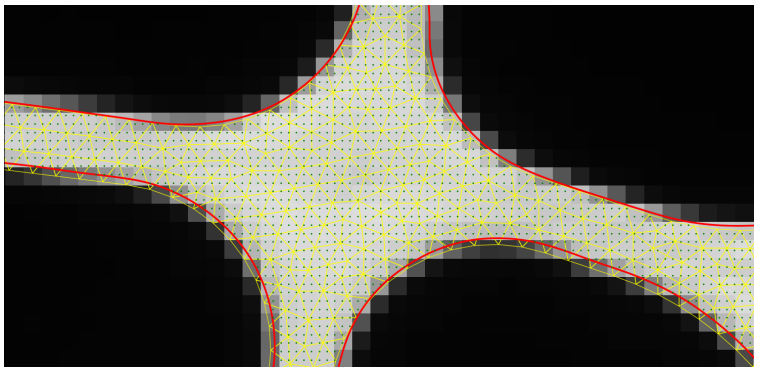

Figure 29: Point cloud belonging to the intersection of the level-set geometry and the FE geometry.

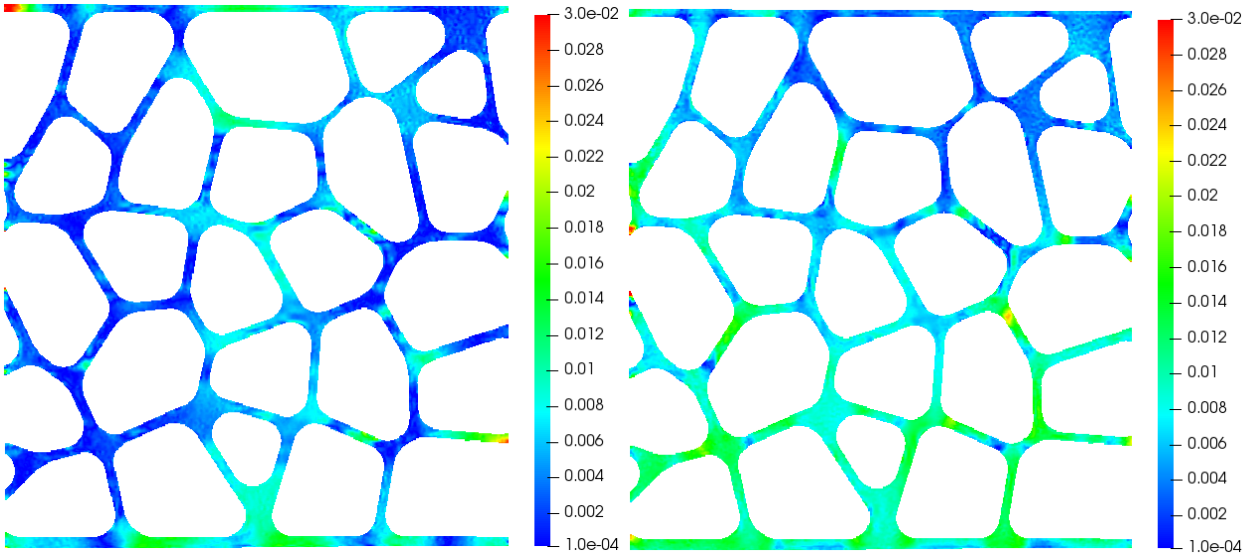

(a) Longitudinal relative error $\frac{|u_x^1 - u_x^2|}{\bar{U}}$.

(b) Transverse relative error $\frac{|u_y^1 - u_y^2|}{\bar{U}}$.

Figure 30: Relative displacement error map between ADDICT (u^1) and FE-DIC measurements (u^2). The difference is scaled by the displacement $\bar{U}$ imposed to the grips.

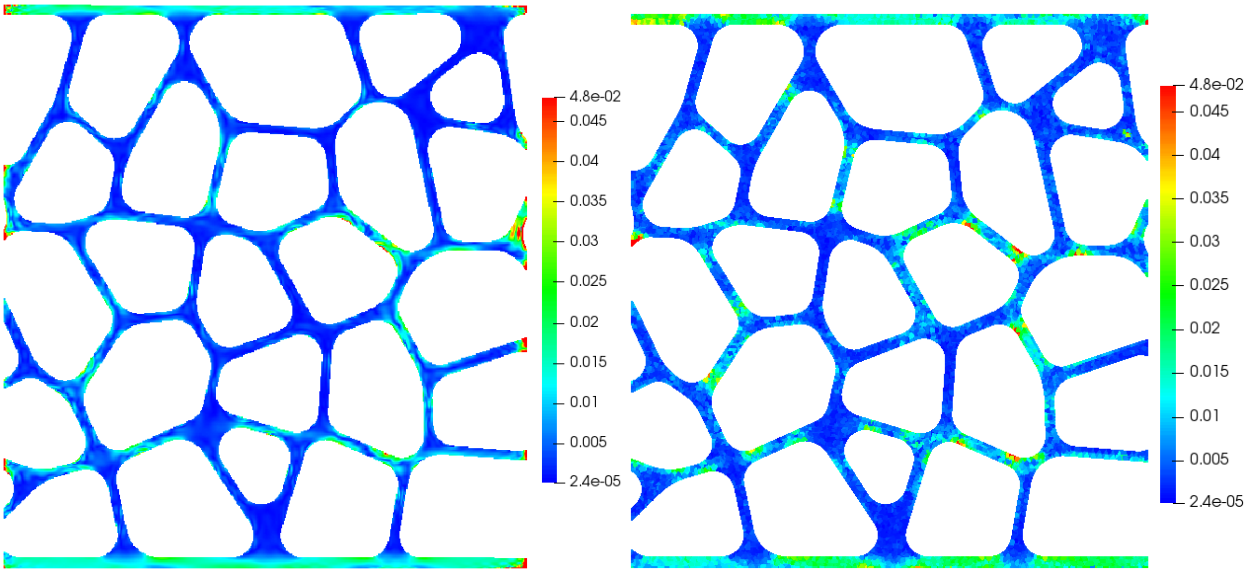

(a) ADDICT measurements with low resolution unspeckled images.

(b) FE-DIC measurement with high resolution speckled images.

Figure 31: Measured Von Mises strain ε_{vm}.

Since the ADDICT measured a relevant displacement field, it becomes possible to validate a simulation by using only the low resolution speckle-free images. Consider, for example, the FE model introduced in section 3.1. The constitutive parameters adopted to describe the elasto-plastic behaviour of the struts are those presented in Table 1. Simple boundary conditions such as those presented in Fig. 7 are adopted. The imposed displacement u_0 is fixed at the value of the measured grips displacement $u_0 = -\bar{U}$. The longitudinal and transverse displacement fields computed with Abaqus are respectively compared to the measurements in Fig. 27 and Fig. 28. The observed differences between the simulated and measured fields are much greater than the difference between the measurement fields. The simulated resultant $\bar{F}$ is also very different from the load measured at this stage (Fig. 24). This means that there is clearly room for an improvement of the simulation (ie. discretization, model, constitutive parameters). Considering that the mesh is sufficiently fine, and that the selected model is relevant, we could consider identifying the constitutive parameters. A classical FEMU approach, such as that proposed by [15], but again based on measurements carried out with speckle-free images, could be adopted. Other identification strategies, entirely in line with

the approach initiated here with ADDICT, could also be adopted [25, 26]. Although fascinating, this topic is beyond the scope of this presentation and would require a separate study.

5. Discussion

As stated in the introduction and reported in many papers of the literature, in the absence of texture at a scale smaller than the cell struts, the grey-scale conservation functional alone is unable to estimate local strains even roughly. Nor can it alone identify a strut that localises more strain than others. On the other hand, this functional makes it possible to estimate the macroscopic component of the displacements provided that any sufficient strong (subset or element size) or weak (Tikhonov like) regularization is used.

In this study, we showed that it is possible to complement this macroscopic estimate obtained by the grey-level functional with an estimate at the microscopic scale by relying weakly on an *a priori* assumption of the underlying physics. Although not limiting, the assumption used here was linear elasticity, even if the observed behaviour was non-linear.

In data assimilation, it is classic to complete a partial measurement with a model. For example, in [43], a stereo measurement is made on the upper (visible) side of a specimen, and the displacements of the lower (non-visible) side are estimated using a model. In a sense, this approach is similar to the one proposed here. More interestingly, the regularization weighting parameter l_K acts as a flexible way to separate the scales: the parts of the displacement of wavelength greater than l_K are handled by the grey-scale metric (if sufficient image gradients) while the ones smaller than l_K by the model.

We provided the numerical evidence that (a) the L-curve technique allows to choose this parameter objectively, (b) the optimal length coincides with the minimum of the true error and (c) the optimal length predicted with this technique is fully consistent with the lengths involved in the architecture of the material studied. It is thus not totally indispensable to go through the L-curve study to find a suitable parameter, since observations of the architecture of the material (with possible computation of the auto-correlation) may be sufficient as a first approach.

By studying numerous synthetic and real test cases, both linear and non-linear, and with the aim of producing, each time, a reliable reference to compare with, we have been able to show that this method provides reliable local information on the distribution of strains. Indeed, even if the reconstructed geometry does not perfectly match the actual specimen geometry, even if the behaviour is not exactly the good one (elastic vs. nonlinear), we have shown that the method allows to estimate complex local kinematic fields (displacements and strains) in a robust way in very poorly defined images and in the absence of texture. More than that, the method allows to identify the distribution of strains in the various struts and the zones within each strut where the strain localises, despite the poorly adapted input data.

An immediate prospect, since ADDICT was built for this purpose, is the extension of this work to DVC to handle real in-situ experiments performed in a μCT scanner [12, 16, 17, 18, 19, 20, 15]. This work is in progress. Such a tool should be undoubtedly valuable for studying the behaviour of a large number of cellular materials (metallic/polymeric foams, bones, wood, additively manufactured lattice structures...). However, the computational cost issue may become a concern in 3D. Domain decomposition techniques or model reduction techniques particularly adapted to the tensor structure of B-splines could then be used advantageously [59, 18, 33]. The DIB model could also be enhanced by other instrumentation modalities (photogrammetry [72], stereo DIC...) A slightly further perspective is the extension of ADDICT to multi-phase materials. Among other perspectives, a very interesting avenue concerns the regularization operator. It is indeed possible, with exactly the same formalism, to consider more advanced models (in particular non-linear ones) [26]. In particular, it would be interesting to update the constitutive parameters of the regularization model, which is possible within the very same framework [25, 26].

Acknowledgements

The authors would like to gratefully thank Laurent Crouzeix for his help during the experiments, Abdallah Bouzid for the fabrication of the samples and Vivien Murat for the speckle deposit.

Funding acknowledgements

This work was supported by *Région Occitanie* and *Université Fédérale Toulouse-Midi-Pyrénées*.

References

[1] M. Ashby, Y. Bréchet, Designing hybrid materials, Acta Materialia 51 (2003) 5801–5821. The Golden Jubilee Issue. Selected topics in Materials Science and Engineering: Past, Present and Future.

[2] Y. Amani, S. Dancette, E. Maire, J. Adrien, J. Lachambre, Two-scale tomography based finite element modeling of plasticity and damage in aluminum foams, Materials 11 (2018).

[3] W. Ludwig, S. Schmidt, E. M. Lauridsen, H. F. Poulsen, X-ray diffraction contrast tomography: a novel technique for three-dimensional grain mapping of polycrystals. I. Direct beam case, Journal of Applied Crystallography 41 (2008) 302–309.

[4] J. C. Plumb, J. F. Lind, J. C. Tucker, R. Kelley, A. D. Spear, Three-dimensional grain mapping of open-cell metallic foam by integrating synthetic data with experimental data from high-energy X-ray diffraction microscopy, Materials Characterization 144 (2018) 448–460.

[5] S. Hollister, J. Brennan, N. Kikuchi, A homogenization sampling procedure for calculating trabecular bone effective stiffness and tissue level stress, Journal of Biomechanics 27 (1994) 433–444.

[6] B. van Rietbergen, H. Weinans, R. Huiskes, A. Odgaard, A new method to determine trabecular bone elastic properties and loading using micromechanical finite-element models, Journal of Biomechanics 28 (1995) 69–81.

[7] J. Homminga, R. Huiskes, B. Van Rietbergen, P. Rüegsegger, H. Weinans, Introduction and evaluation of a gray-value voxel conversion technique, Journal of Biomechanics 34 (2001) 513–517.

[8] A. Düster, H.-G. Sehlhorst, E. Rank, Numerical homogenization of heterogeneous and cellular materials utilizing the finite cell method, Computational Mechanics 50 (2012) 413–431.

[9] C. Verhoosel, G. van Zwieten, B. van Rietbergen, R. de Borst, Image-based goal-oriented adaptive isogeometric analysis with application to the micro-mechanical modeling of trabecular bone, Computer Methods in Applied Mechanics and Engineering 284 (2015) 138 – 164. Isogeometric Analysis Special Issue.

[10] J.-Y. Buffiere, E. Maire, J. Adrien, J.-P. Masse, E. Boller, In situ experiments with X ray tomography: an attractive tool for experimental mechanics, Experimental mechanics 50 (2010) 289–305.

[11] A. Gustafsson, N. Mathavan, M. J. Turunen, J. Engqvist, H. Khayyeri, S. A. Hall, H. Isaksson, Linking multiscale deformation to microstructure in cortical bone using in situ loading, digital image correlation and synchrotron X-ray scattering, Acta Biomaterialia 69 (2018) 323–331.

[12] B. K. Bay, T. S. Smith, D. P. Fyhrie, M. Saad, Digital volume correlation: three-dimensional strain mapping using X-ray tomography, Experimental mechanics 39 (1999) 217–226.

[13] R. Zauel, Y. Yeni, B. Bay, X. Dong, D. P. Fyhrie, Comparison of the linear finite element prediction of deformation and strain of human cancellous bone to 3d digital volume correlation measurements, Journal of biomechanical engineering 128 (2006) 1–6.

[14] E. Dall'Ara, D. Barber, M. Viceconti, About the inevitable compromise between spatial

resolution and accuracy of strain measurement for bone tissue: A 3d zero-strain study, Journal of Biomechanics 47 (2014) 2956–2963.

[15] F. Xu, Quantitative characterization of deformation and damage process by digital volume correlation: A review, Theoretical and Applied Mechanics Letters 8 (2018) 83–96.

[16] H. Leclerc, J.-N. Périé, S. Roux, F. Hild, Voxel-scale digital volume correlation, Experimental Mechanics 51 (2011) 479–490.

[17] H. Leclerc, J.-N. Périé, F. Hild, S. Roux, Digital volume correlation: what are the limits to the spatial resolution?, Mechanics & Industry 13 (2012) 361–371.

[18] L. Gomes Perini, J.-C. Passieux, J.-N. Périé, A multigrid PGD-based algorithm for volumetric displacement fields measurements, Strain 50 (2014) 355–367.

[19] E. Dall'Ara, M. Peña-Fernández, M. Palanca, M. Giorgi, L. Cristofolini, G. Tozzi, Precision of digital volume correlation approaches for strain analysis in bone imaged with micro-computed tomography at different dimensional levels, Frontiers in Materials 4 (2017) 31.

[20] A. Patera, S. Carl, M. Stampanoni, D. Derome, J. Carmeliet, A non-rigid registration method for the analysis of local deformations in the wood cell wall, Advanced structural and chemical imaging 4 (2018) 1–11.

[21] J.-C. Passieux, J.-N. Périé, P. Marguerès, B. Douchin, L. Gomes Perini, On the joint use of an opacifier and digital volume correlation to measure micro-scale volumetric displacement fields in a composite, in: ICTMS2013 - The 1st International Conference on Tomography of Materials and Structures, Ghent, Belgium, 2013.

[22] R. Brault, A. Germaneau, J.-C. Dupré, P. Doumalin, S. Mistou, M. Fazzini, In-situ analysis of laminated composite materials by X-ray micro-computed tomography and digital volume correlation, Experimental Mechanics 53 (2013) 1143–1151.

[23] A. Rouwane, R. Bouclier, J.-C. Passieux, J.-N. Périé, Adjusting fictitious domain parameters for fairly priced image-based modeling: Application to the regularization of digital image correlation, Computer Methods in Applied Mechanics and Engineering 373 (2021) 113507.

[24] J. Réthoré, S. Roux, F. Hild, An extended and integrated digital image correlation technique applied to the analysis of fractured samples, European Journal of Computational Mechanics 18 (2009) 285–306.

[25] J. Réthoré, A fully integrated noise robust strategy for the identification of constitutive laws from digital images, International Journal for Numerical Methods in Engineering 84 (2010) 631–660.

[26] J. Réthoré, Muhibullah, T. Elguedj, M. Coret, P. Chaudet, A. Combescure, Robust identification of elasto-plastic constitutive law parameters from digital images using 3d kinematics, International Journal of Solids and Structures 50 (2013) 73–85.

[27] P. C. Hansen, The L-curve and its use in the numerical treatment of inverse problems, in: in Computational Inverse Problems in Electrocardiology, ed. P. Johnston, Advances in Computational Bioengineering, WIT Press, 2000, pp. 119–142.

[28] Y. Sun, J. H. Pang, C. K. Wong, F. Su, Finite element formulation for a digital image correlation method, Applied optics 44 (2005) 7357–7363.

[29] G. Besnard, F. Hild, S. Roux, "Finite-element" displacement fields analysis from digital images : application to Portevin-Le Châtelier bands, Experimental Mechanics 46 (2006) 789–804.

[30] J. Réthoré, T. Elguedj, P. Simon, M. Coret, On the use of nurbs functions for displacement derivatives measurement by digital image correlation, Experimental Mechanics 50 (2010) 1099–1116.

[31] J.-E. Dufour, B. Beaubier, F. Hild, S. Roux, CAD-based displacement measurements with stereo-DIC, Experimental Mechanics 55 (2015) 1657–1668.

[32] J.-C. Passieux, R. Bouclier, J.-N. Périé, A space-time PGD-DIC algorithm, Experimental Mechanics 58 (2018) 1195–1206.

[33] R. Bouclier, J.-C. Passieux, A domain coupling method for finite element digital image correlation with mechanical regularization: Application to multiscale measurements and parallel computing, International Journal for Numerical Methods in Engineering 111 (2017) 123–143.

[34] A. Mendoza, J. Neggers, F. Hild, S. Roux, Complete mechanical regularization applied to digital image and volume correlation, Computer Methods in Applied Mechanics and Engineering 355 (2019) 27–43.

[35] D. Schillinger, M. Ruess, The finite cell method: A review in the context of higher-order structural analysis of CAD and image-based geometric models, Archives of Computational Methods in Engineering 22 (2015) 391–455.

[36] B. K. P. Horn, B. G. Schunck, Determining optical flow, Artif. Intell. 17 (1981) 185–203.

[37] M. Unser, Splines: a perfect fit for signal and image processing, IEEE Signal Processing Magazine 16 (1999) 22–38.

[38] B. D. Lucas, T. Kanade, et al., An iterative image registration technique with an application to stereo vision, Vancouver, British Columbia, 1981.

[39] M. A. Sutton, W. Wolters, W. Peters, W. Ranson, S. McNeill, Determination of displacements using an improved digital correlation method, Image and vision computing 1 (1983) 133–139.

[40] M. A. Sutton, S. R. McNeill, J. D. Helm, Y. J. Chao, Advances in two-dimensional and three-dimensional computer vision, Photomechanics (2000) 323–372.

[41] D. Garcia, J.-J. Orteu, 3d deformation measurement using stereo-correlation applied to experimental mechanics, in: Proceedings of the 10th FIG international symposium deformation measurements, Orange, CA, 2001, pp. 19–22.

[42] R. Fedele, L. Galantucci, A. Ciani, Global 2d digital image correlation for motion estimation in a finite element framework: a variational formulation and a regularized, pyramidal, multi-grid implementation, International Journal for Numerical Methods in Engineering 96 (2013) 739–762.

[43] J.-E. Pierré, J.-C. Passieux, J.-N. Périé, Finite Element Stereo Digital Image Correlation: framework and mechanical regularization, Experimental Mechanics 57 (2017) 443–456.

[44] L. Wittevrongel, P. Lava, S. V. Lomov, D. Debruyne, A self adaptive global digital image correlation algorithm, Experimental Mechanics 55 (2015) 361–378.

[45] T. W. Sederberg, S. R. Parry, Free-form deformation of solid geometric models, in: Proceedings of the 13th annual conference on Computer graphics and interactive techniques, 1986, pp. 151–160.

[46] R. Szeliski, S. Lavallée, Matching 3-d anatomical surfaces with non-rigid deformations using octree-splines, International journal of computer vision 18 (1996) 171–186.

[47] D. Rueckert, L. I. Sonoda, C. Hayes, D. L. G. Hill, M. O. Leach, D. J. Hawkes, Non-rigid registration using free-form deformations: application to breast mr images, IEEE Transactions on Medical Imaging 18 (1999) 712–721.

[48] G. Colantonio, M. Chapelier, R. Bouclier, J.-C. Passieux, E. Marenić, Noninvasive multilevel geometric regularization of mesh-based three-dimensional shape measurement, International Journal for Numerical Methods in Engineering 121 (2020) 1877–1897.

[49] J.-C. Passieux, R. Bouclier, Classic and inverse compositional gauss-newton in global DIC, International Journal for Numerical Methods in Engineering 119 (2019) 453–468.

[50] J. Neggers, B. Blaysat, J. P. M. Hoefnagels, M. G. D. Geers, On image gradients in digital image correlation, International Journal for Numerical Methods in Engineering 105 (2016) 243–260.

[51] J.-C. Passieux, F. Bugarin, C. David, J.-N. Périé, L. Robert, Multiscale displacement field measurement using digital image correlation: Application to the identification of elastic properties, Experimental Mechanics 55 (2015) 121–137.

[52] M. A. Sutton, J. J. Orteu, H. Schreier, Image correlation for shape, motion and deformation measurements: basic concepts, theory and applications, Springer Science & Business Media, 2009.

[53] M. Bornert, F. Brémand, P. Doumalin, J.-C. Dupré, M. Fazzini, M. Grédiac, F. Hild, S. Mistou, J. Molimard, J.-J. Orteu, et al., Assessment of digital image correlation measurement errors: methodology and results, Experimental mechanics 49 (2009) 353–370.

[54] E. Jones, M. Iadicola, A Good Practices Guide for Digital Image Correlation, International Digital Image Correlation Society, 2018.

[55] A. Tarantola, Inverse problem theory and methods for model parameter estimation, SIAM, 2005.

[56] D. Rueckert, L. I. Sonoda, C. Hayes, D. L. Hill, M. O. Leach, D. J. Hawkes, Non-rigid registration using free-form deformations: application to breast mr images, IEEE transactions on medical imaging 18 (1999) 712–721.

[57] R.-c. Yang, A regularized finite-element digital image correlation for irregular displacement field, Optics and Lasers in Engineering 56 (2014) 67–73.

[58] N. P. van Dijk, D. Wu, C. Persson, P. Isaksson, A global digital volume correlation algorithm based on higher-order finite elements: Implementation and evaluation, International Journal of Solids and Structures 168 (2019) 211–227.

[59] J.-C. Passieux, J.-N. Périé, High resolution digital image correlation using Proper Generalized Decomposition: PGD-DIC, International Journal for Numerical Methods in Engineering 92 (2012) 531–550.

[60] J.-E. Dufour, S. Leclercq, J. Schneider, S. Roux, F. Hild, 3d surface measurements with isogeometric stereocorrelation—application to complex shapes, Optics and Lasers in Engineering 87 (2016) 146–155.

[61] D. Z. Turner, R. B. Lehoucq, C. A. Garavito-Garzón, PDE Constrained Optimization for Digital Image Correlation., Technical Report, Sandia National Lab.(SNL-NM), Albuquerque, NM (United States), 2015.

[62] D. Claire, F. Hild, S. Roux, A finite element formulation to identify damage fields: the equilibrium gap method, International journal for numerical methods in engineering 61 (2004) 189–208.

[63] T. Zvonimir, F. Hild, S. Roux, Mechanical-aided digital images correlation, Strain Analysis 48 (2013) 330–343.

[64] J. Liu, N. Vanderesse, J.-C. Stinville, T. Pollock, P. Bocher, D. Texier, IN-PLANE and out-of-plane deformation at the SUB-GRAIN scale in polycrystalline materials assessed by confocal microscopy, Acta Materialia 169 (2019) 260–274.

[65] J. Parvizian, A. Düster, E. Rank, Finite cell method, Computational Mechanics 41 (2007) 121–133.

[66] B. Pan, Bias error reduction of digital image correlation using gaussian pre-filtering, Optics and Lasers in Engineering 51 (2013) 1161–1167.

[67] C. L. Chan, C. Anitescu, Y. Zhang, T. Rabczuk, Two and three dimensional image registration based on b-spline composition and level sets, Communications in Computational Physics 21 (2017) 600–622.

[68] J.-J. Orteu, D. Garcia, L. Robert, F. Bugarin, A speckle texture image generator, in: Speckle06: speckles, from grains to flowers, volume 6341, International Society for Optics and Photonics, 2006, p. 63410H.

[69] F. Sur, B. Blaysat, M. Grediac, Rendering deformed speckle images with a boolean model, Journal of Mathematical Imaging and Vision 60 (2018) 634–650.

[70] J. Neggers, F. Mathieu, F. Hild, S. Roux, N. Swiergiel, Improving full-field identification using progressive model enrichments, International Journal of Solids and Structures 118-119 (2017) 213–223.

[71] J.-C. Passieux, An open source FE-DIC library, `https://github.com/jcpassieux/pyxel`, 2018. doi:`10.5281/zenodo.4654018`.

[72] S. Heinze, T. Bleistein, A. Düster, S. Diebels, A. Jung, Experimental and numerical investigation of single pores for identification of effective metal foams properties, Zeitschrift Angewandte Mathematik und Mechanik 98 (2018) 682–695.